

Low-Wavenumber Structure and Evolution of the Hurricane Inner Core Observed by Airborne Dual-Doppler Radar

PAUL D. REASOR AND MICHAEL T. MONTGOMERY

Department of Atmospheric Science, Colorado State University, Fort Collins, Colorado

FRANK D. MARKS JR. AND JOHN F. GAMACHE

NOAA/AOML, Hurricane Research Division, Miami, Florida

(Manuscript received 3 May 1999, in final form 30 July 1999)

ABSTRACT

The asymmetric dynamics of the hurricane inner-core region is examined through a novel analysis of high temporal resolution, three-dimensional wind fields derived from airborne dual-Doppler radar. Seven consecutive composites of Hurricane Olivia's (1994) wind field with 30-min time resolution depict a weakening storm undergoing substantial structural changes. The symmetric and asymmetric mechanisms involved in this transformation are considered separately.

To zeroth order the weakening of the primary circulation is consistent with the axisymmetric vortex spindown theory of Eliassen and Lystad for a neutrally stratified atmosphere. Vertical shear, however, increased dramatically during the observation period, leading to a strong projection of the convection onto an azimuthal wavenumber 1 pattern oriented along the maximum vertical shear vector. Recent theoretical ideas elucidating the dynamics of vortices in vertical shear are used to help explain this asymmetry.

The role of asymmetric vorticity dynamics in explaining some of the physics of hurricane intensity change motivates a special focus on Olivia's vorticity structure. It is found that an azimuthal wavenumber 2 feature dominates the asymmetry in relative vorticity below 3-km height. The characteristics of this asymmetry deduced from reflectivity and wind composites during a portion of the observation period show some consistency with a wavenumber 2 discrete vortex Rossby edge wave. Barotropic instability is suggested as a source for the wavenumber 2 asymmetry through a series of barotropic numerical simulations.

Trailing bands of vorticity with radial wavelengths of 5–10 km are observed in the inner core approximately 20 km from the storm center, and may be symmetrizing vortex Rossby waves. Elevated reflectivity bands with radial scales comparable to those of the vorticity bands, also near 20–25-km radius, may be associated with these vorticity features.

1. Introduction

Hurricane intensity is influenced by the properties of the surface, interaction with the environmental flow, and the internal vortex dynamics. It is well known that in the event surface fluxes of latent heat are diminished, as is generally the case when cold sea surface temperatures (SST) or land are encountered, the hurricane vortex spins down. The import of latent heat energy into the core is necessary for sustaining convection and maintaining the intensity of a mature storm.

Fluctuations in intensity are often ascribed to changes in SSTs and the vertical shear of environmental winds, eyewall cycles, or trough interactions (Simpson and Riehl 1958; Black and Willoughby 1992; Molinari et al. 1995; Shay et al. 1998). Recently the asymmetric

vorticity dynamics of the hurricane near-core region also has been examined for its potential role in intensity change. Montgomery and Kallenbach (1997, hereafter MK) showed that symmetrizing vorticity perturbations embedded in the primary vortex circulation can lead to mean flow changes, and that the basic mechanics of this interaction, or "axisymmetrization," is captured by linear vortex Rossby wave theory. Montgomery and Enagonio (1998) validated these predictions for small, but finite-amplitude, vorticity disturbances in a barotropic nondivergent model and then applied the theory to the problem of tropical cyclogenesis at order-one wave amplitudes. The latter study demonstrated how three-dimensional axisymmetrization of convectively generated potential vorticity (PV) anomalies near a weak midlevel parent vortex can lead to the spinup of a cyclonic circulation near the surface. The development of a warm-core vortex was found to be a natural by-product of axisymmetrization. As Fig. 1 shows for Hurricane Olivia (1994), the symmetric component of wind magni-

Corresponding author address: Paul D. Reasor, Dept. of Atmospheric Science, Colorado State University, Fort Collins, CO 80523.
E-mail: reasor@eady.atmos.colostate.edu

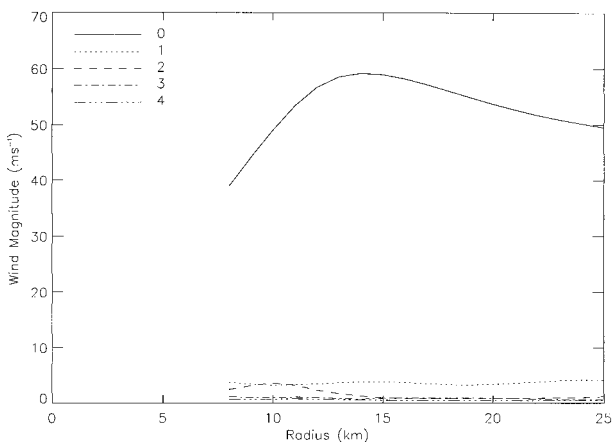


FIG. 1. Hurricane Olivia (1994) dual-Doppler-derived wind magnitude (m s^{-1}) at 1.5-km height averaged over the observation period. Shown are the symmetric, azimuthal wavenumber 1, wavenumber 2, wavenumber 3, and wavenumber 4 components. The "no scatter" region of the eye (i.e., within approximately 8-km radius) is blocked out here and in subsequent plots.

tude in the inner-core region in the lower to middle troposphere can be an order of magnitude greater than the higher wavenumber contributions (see also Fig. 1 of Shapiro and Montgomery 1993). Thus, in the absence of strong flow instability, linear theory and its wave-mean predictions should give useful qualitative insight into the vorticity dynamics of the near-core region and internally generated intensity change.

The nonlinear vorticity dynamics of the hurricane core region has also received attention in the work of Schubert et al. (1999, hereafter S99). They proposed that during periods in which convective forcing is weakened or suppressed altogether the breakdown of the PV ring encircling the hurricane eye via barotropic instability will promote mixing in the eye region, thereby influencing the eye dynamics and thermodynamics. As part of the breakdown process, eyewall mesovortices were predicted to form. These secondary vortices may have local wind speeds that exceed that of the symmetric circulation, increasing locally the destructive potential of the hurricane (Black and Marks 1991; Hasler et al. 1997).

While the vorticity dynamics of the hurricane's near-core region has been the subject of recent numerical and theoretical studies (Guinn and Schubert 1993; MK; S99), it has yet to be explored in great observational detail. This may be, in part, a consequence of the complications that convection provides to the idealized dynamical theories described above, but is also likely a result of inadequate observations of the hurricane near-core evolution. The first airborne Doppler radar study of the tropical cyclone wind structure was reported by Marks and Houze (1984) for Hurricane Debby (1982). Small-scale eddies embedded in the primary circulation were observed, as well as an apparent mesocyclone and its attendant low-level vorticity. They speculated that

advection of the mesocyclone vorticity into the storm core by the radial inflow might influence storm development. A more complete three-dimensional mapping of the hurricane wind field, including the vertical wind, was performed by Marks et al. (1992, hereafter MHG) for Hurricane Norbert (1984). Only a single wind composite spanning roughly 2 h was made, so information on the time evolution of the three-dimensional wind field was unavailable. Nevertheless, with an average time separation of about 7.5 min between measurement of orthogonal components of the horizontal wind, details of the mesoscale structure of the eyewall could be provided in each individual quadrant of the storm. At 3-km height and above they observed a cyclonic and anticyclonic vortex couplet in the flow field with maximum amplitude at the radius of maximum tangential wind (RMW). Individual changes in and the interaction between the mean horizontal flow and this vortex couplet were discussed as possible mechanisms for intensity change.

In this paper we examine seven consecutive wind composites derived from dual-Doppler measurements of Hurricane Olivia (1994) spanning a 3.5-h period, documenting the evolution of the inner core. Roux and Viltard (1995) had available a similar set of data for Hurricane Claudette (1991) spanning a period of about 7 h. The extended velocity track display method used to construct their wind fields, however, resolved only azimuthal wavenumbers 0, 1, and 2 in tangential wind, and wavenumbers 0 and 1 in radial wind (Roux and Marks 1996). In section 5 wavenumber 2 in vorticity is shown to be a dominant flow feature at low levels in Olivia, so such a restriction is not acceptable in this case.

Our primary aim here is to determine the extent to which the dual-Doppler data can be used to elucidate the inner-core asymmetric vorticity dynamics of the hurricane. In section 2 we discuss the history of Hurricane Olivia (1994) and the data used in this study. To provide context for the discussion of the vorticity dynamics we first examine Olivia's symmetric evolution in section 3 and interaction with vertical shear in section 4. In section 5 we then present the structure and evolution of Olivia's vorticity, including evidence for an azimuthal wavenumber 2 vortex Rossby wave mode propagating around the eyewall. Possible sources for this asymmetry are discussed. Bands of vorticity also appear in the wind field snapshots and may be the sheared vortex Rossby waves discussed above as playing a role in the structural evolution of the hurricane near core.

2. Data

a. Hurricane Olivia on 25 September 1994

Eastern Pacific storm Olivia strengthened into a hurricane near 15°N and 115°W on 24 September 1994. According to Pasch and Mayfield (1996), Olivia con-

tinued to strengthen on 24 September, reaching a minimum surface pressure of 949 mb by the end of the day. SSTs were approximately 28°C (Gamache et al. 1997). Peak intensity was observed around 1200 UTC on 25 September with sustained tangential wind speeds of approximately 67 m s⁻¹. Following this time Olivia fell under the influence of a mid- to upper-tropospheric cyclone west of southern California, resulting in a 4–5 m s⁻¹ northward storm motion. Late on 25 September two National Oceanic and Atmospheric Administration (NOAA) Aircraft Operations Center (AOC) WP-3D research aircraft flew through Hurricane Olivia. The eyewall reflectivity was found to be axisymmetric at the beginning of the observation period, and to evolve into a highly asymmetric distribution over the following 4 h (Fig. 2). As Olivia continued to move north-northeast under increasing southwesterly vertical shear and somewhat cooler SSTs (~27°C), the winds gradually weakened to tropical storm strength late on 26 September.

b. Radar observation of Hurricane Olivia

Two NOAA AOC WP-3D aircraft equipped with Doppler radar flew simultaneous, near-orthogonal flight tracks through the inner core of Hurricane Olivia on 25 September 1994. Seven consecutive flight legs through the eye were made during the period 2027–2355 UTC (see Table 1 for details). Dual-Doppler coverage was available out to a radius of 30 km from the storm center.

Horizontal scans of radar reflectivity obtained from the lower fuselage (LF) C-band (5.5-cm wavelength) radar antenna of the lower aircraft are used in section 5 to look at the fine-timescale evolution of Olivia's inner core. Throughout the rest of the paper three-dimensional composites of reflectivity from the tail (TA) X-band (3.2-cm wavelength) radar antenna, which scans perpendicular to the aircraft ground track, are used to show the reflectivity evolution over the 3.5-h observation period. Further details of the TA and LF radars are provided by Jorgensen (1984). The method of TA radar reflectivity compositing is discussed by Marks and Houze (1984).

The use of two TA radar platform allows for a true dual-Doppler sampling technique to be employed. The upper and lower aircraft fly orthogonal legs through the hurricane inner core, providing near-simultaneous measurements of orthogonal components of the horizontal wind over a period of 10–15 min. In the two quadrants of the storm where the TA radar beams intersect, the average time separation between measurement of the horizontal wind components is 2.7 min. In the other two quadrants of the storm an average time separation of 6 min exists. The time between three-dimensional samplings of the inner-core wind field is roughly 20 min. Seven consecutive wind composites were constructed for the 3.5-h observation period.

The conventional method for obtaining three-dimensional wind fields from raw Doppler radials is to first

solve the two dual-Doppler projection equations for zonal and meridional velocity using an estimate for the total vertical velocity. The anelastic continuity equation is then integrated vertically to obtain the vertical air velocity, which is used to recompute the horizontal winds. An iterative procedure is followed until a convergence criterion is met (e.g., MHG). The wind fields used in this study were created through a refinement to the above technique. A variational method outlined by Gamache (1998) was employed in which the dual-Doppler equations and continuity equation are solved simultaneously. According to Gamache (1998) this method should be more stable than the conventional method for Doppler radials with high incidence angle (i.e., large elevation angles from the horizontal).

The domain of the TA wind and reflectivity composites extends 30 km from the storm center in the horizontal and from 0.75 to 6 km in the vertical. Data above 6-km height are available, but not used (except in the calculation of area-average horizontal wind discussed in section 4). The filtering of the dual-Doppler data used in this study is not uniform in space. This is in large part a consequence of the difference in tangential and radial velocity found in a hurricane. Between Doppler wind measurements at a point in space, features in the wind field are advected much greater distances in the azimuth than in the radial. During the average time separation between measurements in the eyewall (~3 min) parcels are advected 5–10 km in the azimuth and 1–2 km in the radial. Thus, we will focus on wave-numbers 0, 1, and 2 in the azimuth and scales ≥ 4 km in the radial.

c. Data quality

The winds derived from the true dual-Doppler sampling of Olivia are compared to the in situ aircraft wind measurements made along the flight tracks at 3-km height. Flight-level wind measurements were smoothed with a 2-km Bartlett filter (M. Eastin 1998, personal communication). Figure 3 shows the flight-level estimate of the wind at a point along the flight track versus the Doppler-derived estimate nearest that point in space. All flight-level points within the dual-Doppler domain are considered, and all seven flight legs are utilized. Good agreement exists for the horizontal components of the wind (Figs. 3a and 3b). The slopes of the linear best fits to the *U* and *V* winds are 0.98 and 1.01, respectively. The correlation coefficient for the *U* fit is 0.98, while for the *V* fit is 0.99. These findings are consistent with those found by MHG for pseudo-dual-Doppler measurements in Hurricane Norbert (1994).

The agreement between aircraft and Doppler-derived vertical velocities is not expected to be as good as found for the horizontal winds. As noted by MHG, the inherent spatial averaging involved in the computation of Doppler-derived vertical velocity from horizontal wind divergence alters the magnitude and location of the ver-

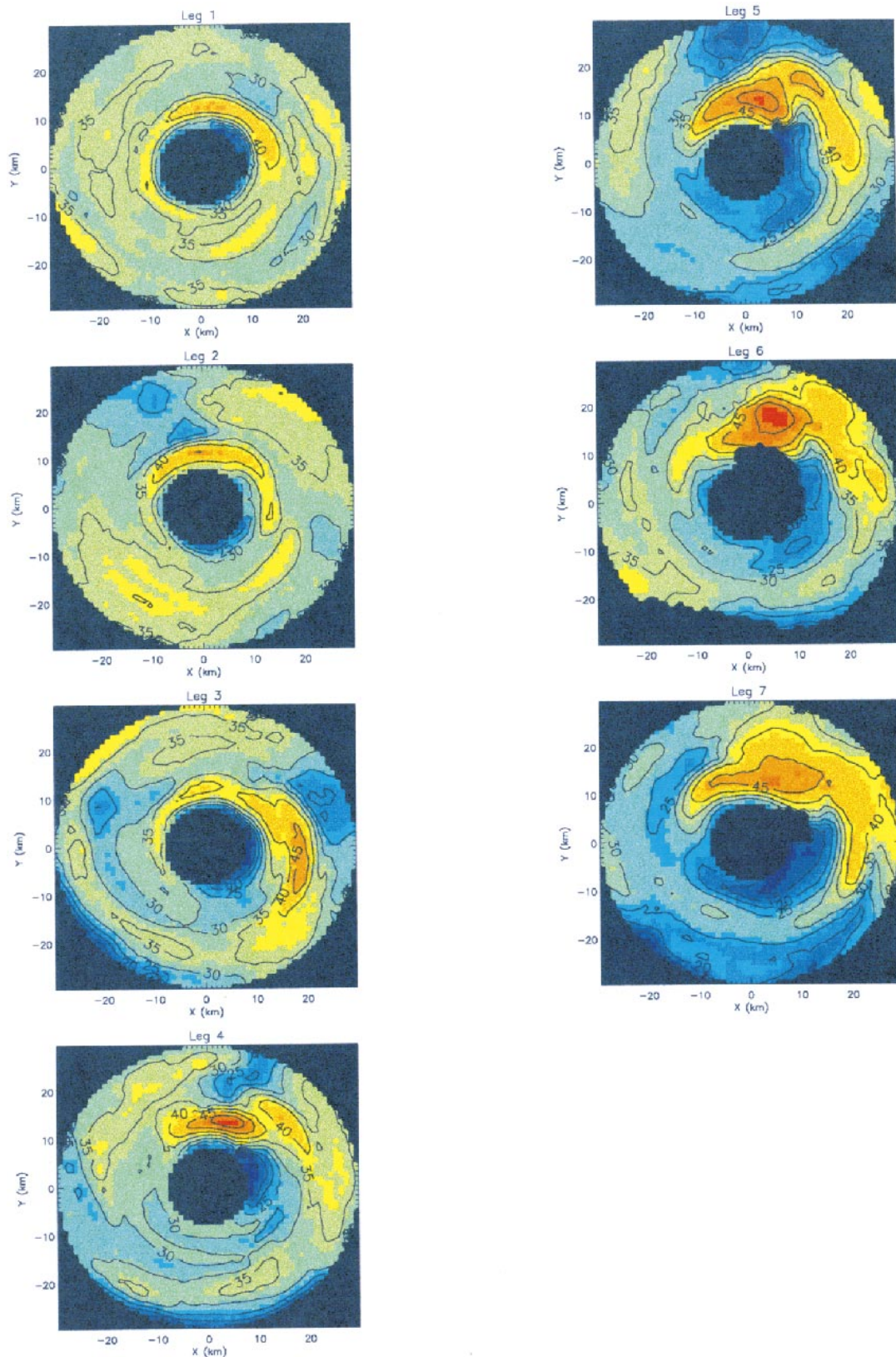


FIG. 2. Composites of Olivia's inner-core reflectivity near 5-km height derived from the TA radars for each flight leg. Contour interval is 5 dBZ. In this and all subsequent horizontal contour plots, geographical north is located at the top of the plot. Note regions of attenuation radially outside the reflectivity maximum in the northern quadrant of the storm.

TABLE 1. Dual-Doppler composite times for the seven flight legs through Hurricane Olivia on 25 Sep 1994, and the NOAA WP-3D aircraft (N42RF at 3-km altitude, N43RF at 4-km altitude) flight tracks through the inner core.

Leg	Composite time (UTC)	N42RF (3 km) flight track	N43RF (4 km) flight track
1	2027–2039	N to S	ENE to W
2	2100–2113	SE to NW	SSW to NNE
3	2132–2143	W to E	N to S
4	2204–2217	NE to SW	SSE to NW
5	2244–2253	S to N	WSW to ENE
6	2310–2330	NW to SE	NNE to SSW
7	2343–2355	E to W	S to N

tical velocity maxima. MHG did find that the *distributions* of vertical velocity for the Doppler and in situ observations in Hurricane Norbert were similar.

d. Wind decomposition

Based on the results of Fig. 1 and other observations of the hurricane near core (e.g., MHG; Franklin et al. 1993) we may regard the hurricane inner-core horizontal winds as a superposition of an axisymmetric tangential flow plus weaker azimuthal perturbations, with weak radial flow above the inflow layer and below the upper-tropospheric outflow layer. In order to focus on the symmetric and asymmetric components of the vortex winds separately, and to obtain insight into the dynamics governing the evolution of these components of the total flow, an azimuthal Fourier decomposition of the wind field is performed. The storm-relative winds (\mathbf{V}_r) are first obtained by subtracting the storm motion from the total (earth relative) winds ($\mathbf{V}_{\text{total}}$):

$$\mathbf{V}_r = \mathbf{V}_{\text{total}} - \mathbf{V}_s, \quad (1)$$

where \mathbf{V}_s is the time-dependent, spatially constant storm motion vector (see Willoughby and Chelmon 1982). The initial wind analysis at each level is centered on the flight-level vortex center at roughly 3-km height. Following MHG, we instead choose to center the vortex at each height at the origin of a common cylindrical coordinate system, thus minimizing the asymmetry due to vortex center mislocation. Because of the general lack of scatterers within the eye, the Doppler-derived wind field within roughly 8 km from the storm center cannot be obtained. A simplex algorithm is used to find the center that maximizes the symmetric component of the tangential winds within an annulus centered on the RMW (Neldar and Mead 1965). Using the newly defined center at each level, \mathbf{V}_r is decomposed into azimuthal mean and perturbation wind components. The perturbation wind field is then Fourier decomposed in azimuth in order to focus on the structure and evolution of the low-wavenumber components.

The asymmetric component of \mathbf{V}_r will contain, in addition to internally generated vortex asymmetries, the environmental flow and asymmetries resulting from the

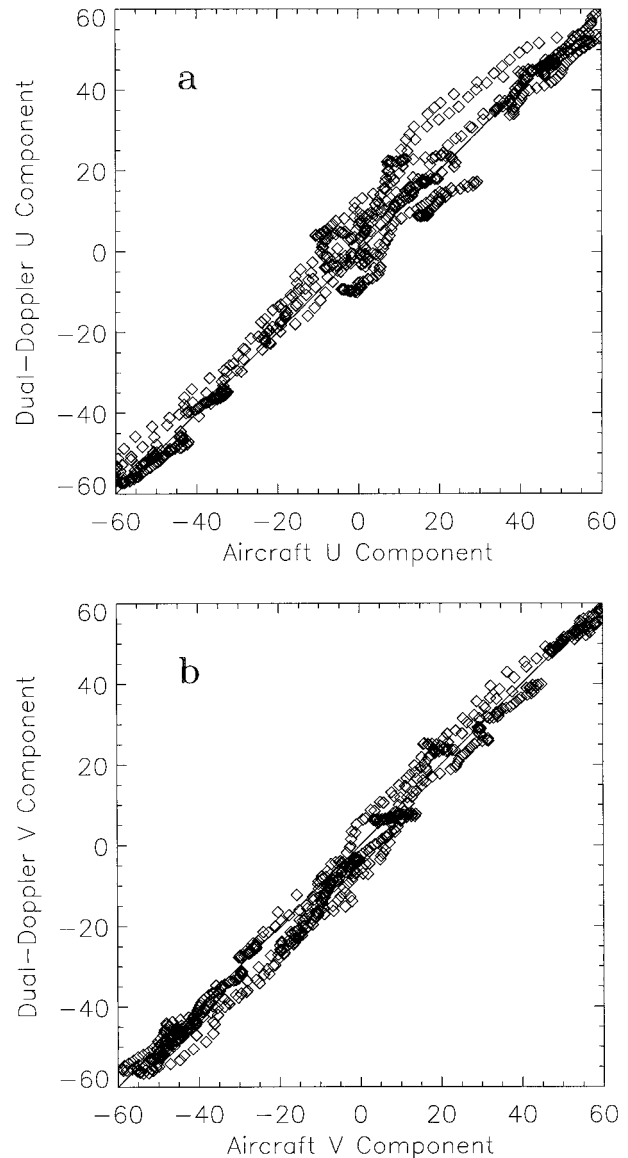


FIG. 3. Point-by-point comparison between aircraft wind measurements at 3-km height during the period 2027–2355 UTC and the Doppler-derived wind estimates nearest in space. The (a) zonal and (b) meridional components of the wind (m s^{-1}) are shown separately. Interpolated data within Olivia's eye are included in the comparison.

interaction of the hurricane with its environment (e.g., upper-level PV anomalies, betagyres, etc.). Consequently, it is not straightforward to simply separate \mathbf{V}_r into environmental and hurricane components. Nevertheless, it proves useful and convenient to define an *estimate* of the environmental vertical shear:

$$\frac{\partial \mathbf{V}_e}{\partial z}(z) = \frac{1}{\pi r_{\text{max}}^2} \int_0^{2\pi} \int_0^{r_{\text{max}}} \frac{\partial \mathbf{V}_{\text{total}}}{\partial z}(r, \lambda, z) r dr d\lambda, \quad (2)$$

where $r_{\text{max}} = 28$ km. This quantity will henceforth be referred to as the local vertical shear. The wind vector \mathbf{V}_e is the area-averaged total wind at each level, which

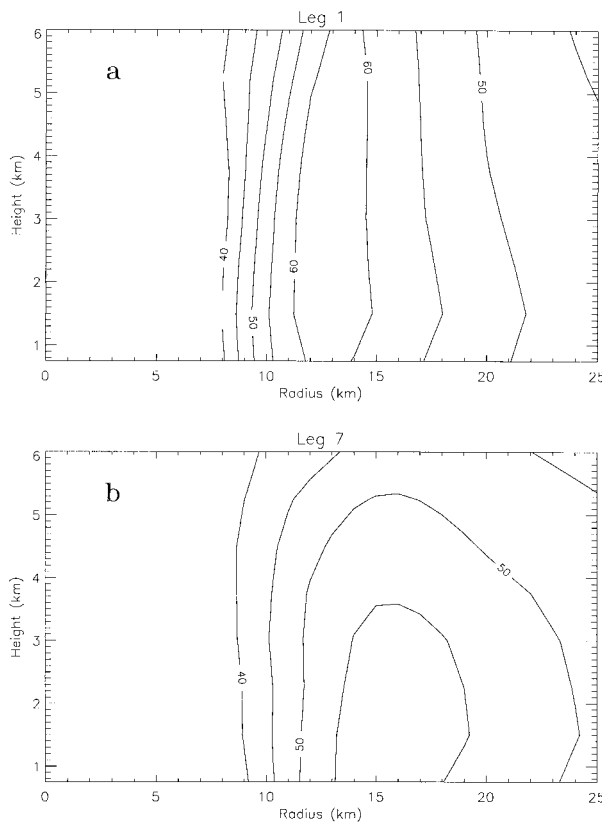


FIG. 4. Radius–height structure of the symmetric tangential winds during (a) leg 1 and (b) leg 7. Contour interval is 5 m s^{-1} .

should contain information on the environmental flow as discussed by MHG for Hurricane Norbert (1984).

3. Symmetric evolution: A weakening storm

Figure 4 shows the symmetric structure of Hurricane Olivia's primary circulation at the beginning (Fig. 4a) and end (Fig. 4b) of the observation period. In the vicinity of the RMW ($\sim 12\text{--}16 \text{ km}$) the tangential winds decrease by $5\text{--}10 \text{ m s}^{-1}$ just above the boundary layer and by a more substantial $10\text{--}20 \text{ m s}^{-1}$ around 6-km height. A near-linear decrease in tangential winds with time is observed near the RMW. The f -plane contributions to the observed tendency in symmetric tangential wind in the inner core are

$$\frac{\partial \bar{v}}{\partial t} = -(f + \bar{\zeta})\bar{u} - \bar{w} \frac{\partial \bar{v}}{\partial z} - \left(\overline{u' \zeta'} + \overline{w' \frac{\partial v'}{\partial z}} \right) + \bar{F}, \quad (3)$$

where u is the radial velocity, v the tangential velocity, w the vertical velocity, f the Coriolis parameter, and ζ the vertical vorticity. The bar denotes an azimuthal average and the prime a departure therefrom. The first two terms are the radial flux of mean vorticity by the mean radial wind and the vertical advection of mean tangential momentum by the mean vertical wind, respectively. The next two terms are the eddy counterparts of the first two

terms, and the last term represents frictional and unresolved effects. The symmetric transverse circulation involved in the first two terms is shown in Fig. 5. Over the observation period the symmetric transverse flow is highly variable. Mechanisms likely involved in the evolution of the secondary circulation include frictional and diabatic forcing, precipitation loading, inertia–gravity wave propagation, and asymmetric vorticity dynamics. It should be noted that the period of pure inertial oscillations in the inner core ranges from 10 to 40 min, which is less than or equal to the time resolution of the data. Thus, the presence of inertia–gravity waves may preclude quantitative, and perhaps qualitative, comparison between observed and budget tendencies from one wind composite to the next.

The role of vorticity asymmetry in producing mean flow change is considered in section 5. Here, we focus on purely symmetric phenomena. A comparison of the left-hand side of (3) and the sum of the first two terms on the right-hand side is shown in Fig. 6 for the flow evolution from legs 1 to 7. Although the observed tangential wind tendency is an order of magnitude less than the budget tendency, qualitative agreement between the two is found. Both depict a negative tendency in the vicinity of the RMW and a positive tendency outside this radius.

Insight into the observed weakening trend in the primary circulation may be obtained using axisymmetric vortex spindown ideas. For an axisymmetric hurricane in approximate gradient and hydrostatic balance the theoretical predictions of Eliassen and Lystad (1977, hereafter EL) are appropriate. Eliassen and Lystad (1977) predicted the decrease in tangential winds with time for a vortex under the influence of a quadratic drag law for the surface stress in a neutrally stratified atmosphere. Figure 1 shows the wind asymmetry to be an order of magnitude smaller than the symmetric wind in the case of Olivia, but measurements of the stratification are unavailable. Neutral buoyancy in the near-core region (excluding the eye) is supported by Emanuel (1986). As long as these assumptions hold approximately true, EL's theory is useful as a zeroth-order description of vortex spindown.

The basic dynamics of vortex spindown are relatively simple. The departure of the flow from exact cyclostrophic balance in the vortex boundary layer due to the presence of frictional drag drives a radial inflow. This radial inflow transports angular momentum into the inner core, compensating for the frictional losses of angular momentum. In the absence of diabatic forcing and the attendant radial inflow above the boundary layer, the free atmosphere radial flow will be outward at all levels (Willoughby 1979). By conservation of angular momentum the tangential winds above the boundary layer must decrease, and the vortex spins down.

The time average of Olivia's symmetric transverse flow over the 3.5-h observation period is shown in Fig. 7. Although inflow is still observed up to 3.5-km height,

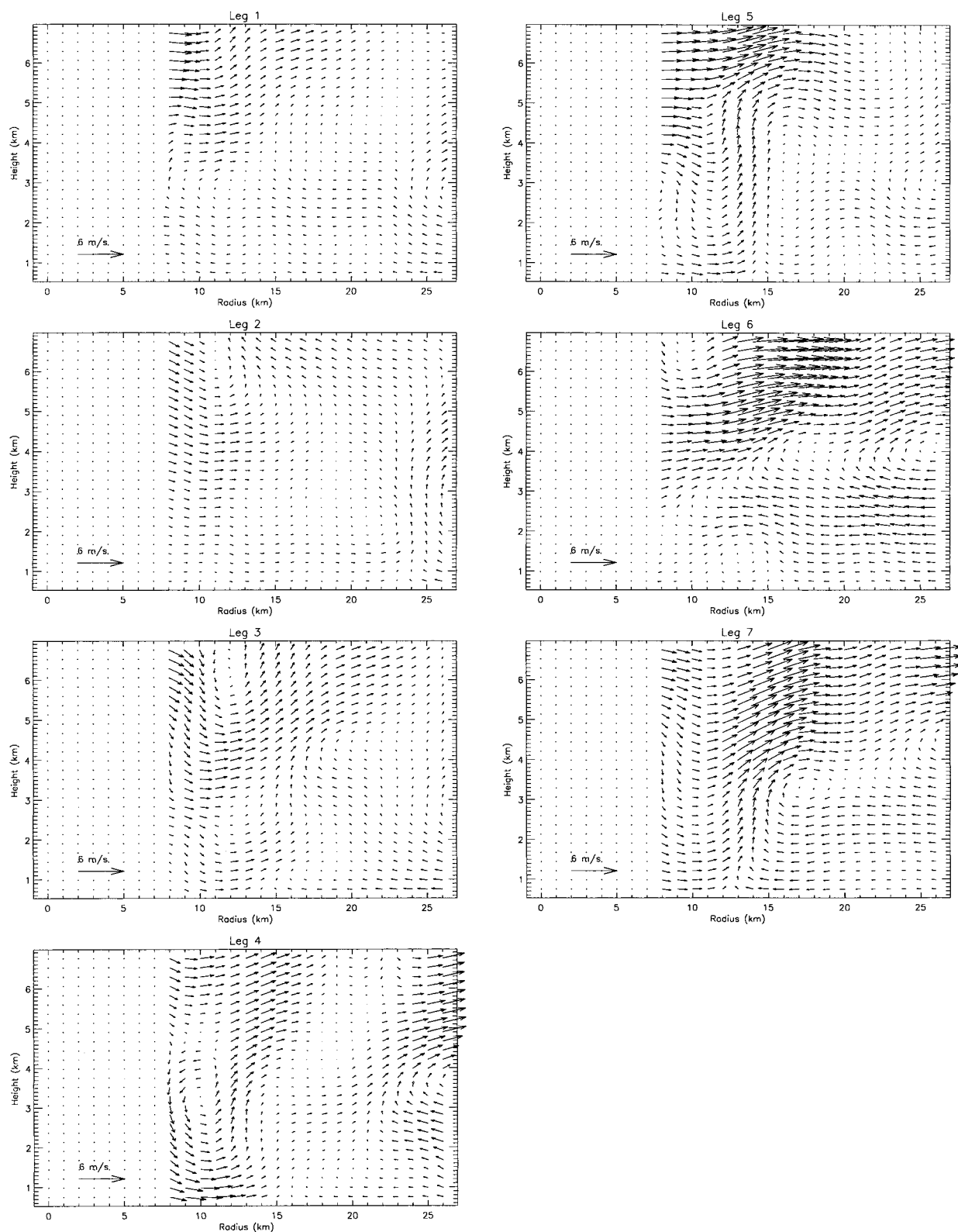


FIG. 5. Radius–height structure of the symmetric transverse flow (u , w) for each flight leg. Wind vectors of the same length, pointing horizontally or vertically, represent the same speed. Maximum wind vector is 6 m s^{-1} .

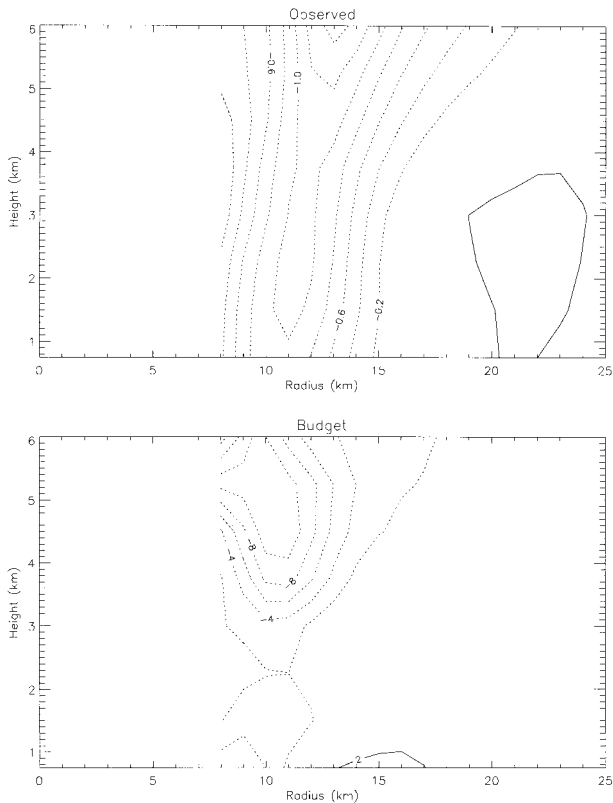


FIG. 6. A comparison between the observed and budget tendencies of symmetric tangential wind for the transition from legs 1 to 7. Only the symmetric radial vorticity flux and vertical advection terms of (3) are used in the budget tendency calculation. The average of the legs 1 and 7 wind fields are used in the budget calculation. Contour intervals for the observed and budget tendencies are $0.2 \times 10^{-3} \text{ m s}^{-2}$ and $2 \times 10^{-3} \text{ m s}^{-2}$, respectively. Negative values are depicted by the dashed curves.

the flow above this level is outward at all radii. This prevalence of radial outflow was also observed by MHG for weakening Hurricane Norbert.

The rate at which the spindown occurs was determined heuristically by EL for weak vortices (maximum tangential winds $\sim 10 \text{ m s}^{-1}$). They used a first-order K theory to parametrize the eddy stresses in the mixed layer and a quadratic drag law for the surface stress. A state of near-cyclostrophic balance was assumed to exist throughout the fluid in an absolute coordinate system. The free atmosphere tangential wind, $v(r, t)$ is given by

$$\frac{1}{|v|} = \frac{1}{|v_0|} + \frac{C_D \chi^2 t}{H - h}, \quad (4)$$

where $|v_0(r)|$ is the initial tangential wind; C_D the assumed constant drag coefficient; χ the ratio of the boundary layer to free atmosphere tangential wind, that is, the reduction factor; H the total depth of the fluid; and h the boundary layer depth. Snell and Montgomery (1999) and Montgomery et al. (2000, manuscript submitted to *J. Atmos. Sci.*) investigated the validity of (4) for hurricane-strength vortices (maximum tangential

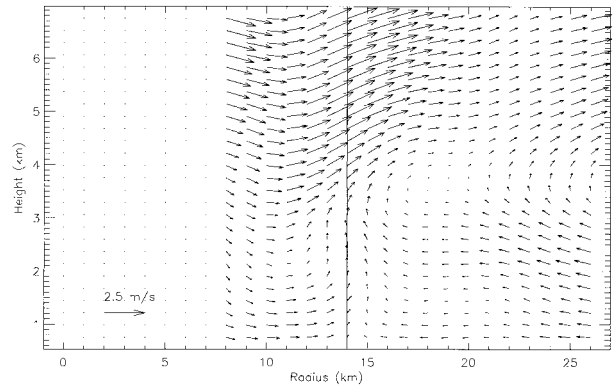


FIG. 7. As in Fig. 5 but averaged over the period 2027–2355 UTC. Maximum wind vector is 2.5 m s^{-1} . The solid line denotes the time-average location of the RMW as a function of height.

winds $\geq 33 \text{ m s}^{-1}$) using an axisymmetric Navier–Stokes model that includes noncyclostrophic terms neglected by EL. They found that the model-derived half-life times of the stronger vortices showed good agreement with the predictions of EL. We therefore use (4) to predict the time evolution of Olivia’s tangential winds above the boundary layer ($\sim 3 \text{ km}$ height) at 12-km radius from the vortex center and compare with the observations. Using the drag coefficient of Deacon (Roll 1965) for 49 m s^{-1} winds in the boundary layer ($\sim 3 \times 10^{-3}$), $H = 15 \text{ km}$, $h = 1 \text{ km}$, $\chi = 0.8$, and $|v_0| = 61 \text{ m s}^{-1}$, we estimate a tangential wind of 58 m s^{-1} during leg 4 and 55 m s^{-1} during leg 7. The observed tangential winds during legs 4 and 7 are approximately 54 and 51 m s^{-1} , respectively. Thus, in spite of the simplifications made in deriving (4) and the greater complexity of Olivia’s environment (e.g., vertical shear), the magnitude of the observed spindown of the tangential winds is consistent with the axisymmetric predictions of EL.

4. Vertical shear dynamics

a. Background

Raymond and Jiang (1990) proposed a mechanism by which the PV anomaly associated with a midlatitude mesoscale convective system interacts with environmental vertical shear to produce enhanced low-level lifting and cumulus convection, thus prolonging the life of the mesoscale convective system. In their conceptual model they assumed that the distortion of the PV anomaly by the vertical shear was negligible. Upward motion then arose downshear as the ambient flow followed the distorted isentropes of the PV anomaly, and the vortex flow followed the tilted ambient isentropes. They estimated that vertical displacements in excess of 500 m could occur over a 24-h period, large enough to release conditional instability. In a subsequent study Raymond (1992) considered the additional effect of distorting the vortex isentropes through tilting by ambient shear. In his simulations he found that the vortex flow on the

distorted isentropes of the tilted vortex produced an important contribution to the vertical motion, with maximum values in the downshear-right quadrant.

The relation between vertical shear and convective asymmetry in hurricanes has been noted observationally (Willoughby et al. 1984; MHG; Franklin et al. 1993) and explored recently using idealized and operational hurricane numerical models (Jones 1995; DeMaria 1996; Bender 1997; Frank and Ritchie 1999). Jones (1995) simulated the evolution of an initially barotropic hurricane-strength vortex in unidirectional vertical shear. The early stages of the simulation produced upward motion downshear via the vortex flow on ambient isentropes and the upward motion of isentropic surfaces as the tilting vortex tried to maintain thermal wind balance. The coupling of upper- and lower-level PV anomalies led to changes in the direction of vortex tilt with respect to the ambient vertical shear vector. As the tilt became more substantial, the pattern of vertical motion was governed increasingly by the vortex flow on distorted isentropes. The maximum upward motion then occurred to the right of the local tilt vector.

Insight into the relative contributions of vertical shear and vortex tilt to the vertical motion pattern may be obtained by first considering the dynamics in a quasi-geostrophic (QG) framework. We begin by defining an initially circular barotropic vortex in pseudoheight coordinates tilted linearly with height in the zonal direction. In Cartesian coordinates the tilted vortex is described as follows:

$$U = \frac{-2Rv_{\max}y}{R^2 + (x - \alpha z)^2 + y^2} \quad \text{and} \quad V = \frac{2Rv_{\max}(x - \alpha z)}{R^2 + (x - \alpha z)^2 + y^2}, \quad (5)$$

where U and V are the zonal and meridional components of the wind, respectively; R the RMW; v_{\max} the maximum tangential wind; and α the constant change in vortex center displacement with height. A vertically sheared zonal environmental wind, U_e , is then added to this vortex wind field, and the total wind field is transformed into a cylindrical coordinate system (r, λ, z) whose origin is the vortex center on the lowest surface, $z = 0$.

The vertical velocity field required to maintain thermal wind balance is obtained by solving the well-known \mathbf{Q} -vector form of the omega equation written in cylindrical coordinates (Hoskins et al. 1978):

$$N^2 \nabla^2 w + f^2 \frac{\partial^2 w}{\partial z^2} = 2 \nabla \cdot \mathbf{Q}, \quad (6)$$

where N is the Brunt–Väisälä frequency, ∇ the horizontal gradient operator, and

$$\mathbf{Q} = \left(f \left[\frac{\partial u}{\partial z} \frac{\partial v}{\partial r} - \frac{\partial u}{\partial r} \frac{\partial v}{\partial z} \right], \frac{f}{r} \left[\frac{\partial u}{\partial z} \left(\frac{\partial v}{\partial \lambda} + u \right) - \frac{\partial v}{\partial z} \left(\frac{\partial u}{\partial \lambda} - v \right) \right] \right), \quad (7)$$

where u and v are the geostrophic radial and tangential winds, respectively. We first substitute the expression for the winds into (7) and then compute the horizontal divergence. A new coordinate system (r', λ', z) is defined with the origin at the center of the displaced vortex at each height (see appendix A for details). Defining a nondimensional radius $b' = r'/R$, the expression for the \mathbf{Q} -vector divergence becomes

$$\nabla \cdot \mathbf{Q} = \frac{16b'f^3\text{Ro}}{R(1 + b'^2)^4} \left[(\alpha\text{Ro})(2 - b'^2) \sin\lambda' - \frac{1}{f} \left(\frac{\partial U_e}{\partial z} \right) (1 + b'^2) \cos\lambda' \right], \quad (8)$$

where $\text{Ro} \equiv v_{\max}/fR$ is the Rossby number. The first term on the right-hand side represents the forcing due to vortex flow on distorted isentropes, while the second term represents the effects of vortex flow on ambient isentropes. Note that in the transformed coordinate system the \mathbf{Q} -vector divergence projects *only* onto wave-number 1. Since w is proportional to $-\nabla \cdot \mathbf{Q}$, it follows that the maximum upward motion due to vortex flow on distorted isentropes occurs to the right of the tilt vector, whereas the upward motion along ambient isentropes occurs downshear, as expected. The radius of maximum \mathbf{Q} -vector divergence and, hence, vertical motion tends to occur around $0.5R$ for this particular vortex profile. If solid-body rotation is used instead inside the RMW, the maximum upward motion moves closer to the RMW.

Although (8) is strictly valid for $\text{Ro} \ll 1$, it can be used to describe the qualitative features of the vertical motion field at near unity Rossby number. As an example of its applicability, we consider the vortex discussed by Trier et al. (1998) in their primitive equation (PE) simulation of the interaction of a mesoscale vortex with environmental vertical shear. Since they initialized their model with a baroclinic vortex different from the barotropic vortex described by (5), we focus primarily on qualitative agreement. At 2.1-km height $R = 30$ km and $\text{Ro} \sim 1.5$. The low-level westerly environmental shear is approximately $2 \times 10^{-3} \text{ s}^{-1}$. If the PV anomaly at each height is simply advected by the mean flow, then $\alpha \sim 3$ after 0.5 h and $\alpha \sim 40$ after 6 h. We find that at 0.5 h the vertical motion downshear near $b' = 0.5$ is approximately three times larger than that to the right of the tilt vector. This is consistent with the simulation of Trier et al., which produced upward motion primarily downshear at this time (see their Fig. 2a). At 6 h, when the vortex tilt is more substantial, we estimate that the upward motion to the right of the tilt vector is about four times greater than the downshear component. This is again consistent with their simulated vertical motion (see their Fig. 2b).

Using the actual initial vortex and environmental flow parameters of Trier et al. in a standard QG omega-equation

tion solver produces a vertical velocity pattern in good agreement with their simulated results at 0.5 and 6 h (not shown). The magnitude of the QG vertical velocity, however, is a factor of 2–3 less than the PE values. Employing a balance theory more appropriate for rapidly rotating vortices would reduce this discrepancy. An equation similar to (6) was derived by Shapiro and Montgomery [1993, Eq. (4.6)] for the asymmetric balance (AB) system valid for hurricane-strength swirling flows. The AB generalization of the QG omega equation may allow one to obtain an expression similar to (8). A more quantitative comparison with PE simulations and actual observations will be investigated in future work.

b. Observed evolution of shear, tilt, and vertical velocity

The observations of Hurricane Olivia on 25 September 1994 provide a unique look at the role of vertical shear in producing structural changes to the inner-core wind field. The seven consecutive wind composites capture for the first time the asymmetric response of a hurricane to dramatic changes in vertical shear over a relatively short time period. Figure 8 shows hodographs of area-averaged storm-relative wind ($\mathbf{V}_e - \mathbf{V}_s$) during the observation period. Figure 9 shows the best estimate of inner-core vortex tilt derived from the simplex algorithm. Initially the maximum local vertical shear over the 0.75–10.5-km depth is weak west-northwesterly, with values on the order of 3–5 m s^{-1} . Consistent with the weak shear, the vortex is nearly vertically aligned. Over the next 2.5 h the maximum shear increases to 15 m s^{-1} and is westerly. A west to east tilt of the vortex with height evolves, with a maximum displacement from low to middle levels of about 3 km. Inspection of the flow field from 6- to 10.5-km height, where the simplex algorithm for finding the vortex center is less reliable, indicates that the inner core does not tilt more than 5 km (not shown).

According to the adiabatic mechanism for vertical velocity production, the preferred location for enhanced convection due to vertical shear effects should be downshear right in the east to southeast quadrant of the storm. Olivia was moving to the north-northeast at about 5 m s^{-1} during this time, so enhanced asymmetric boundary layer convergence and, hence, convection might also be expected in the north-northeast quadrant (Shapiro 1983). Figure 10 shows an azimuth–height cross-section of vertical velocity in Olivia’s inner core at 14-km radius. The upward velocity is generally maximum downshear during legs 1 and 2, and consistent with the weak vertical shear during this time the values are smaller than observed during latter legs. The front to back convective asymmetry discussed by Shapiro (1983) is not apparent during the small shear–tilt period. It may exist at low levels unresolved in the present analysis.

As the vertical shear and vortex tilt increase, the max-

imum upward velocity increases from 1–2 to 6–10 m s^{-1} and the pattern of convection becomes more complicated. A “double maximum” in upward motion develops on the downshear side of the vortex with one maximum downshear left and the other downshear right. The downshear-left maximum tends to be the stronger of the two. The storm motion during the period from leg 1 to leg 7 is relatively steady and the direction of motion changes gradually by only 10° , so it is unlikely that the dramatic *changes* in vertical motion could be attributed to the asymmetric boundary layer convergence described by Shapiro (1983).

The observed trend of increased upward motion downshear and downshear right with increased vertical shear and vortex tilt is consistent with the adiabatic mechanisms discussed in section 4a. Frank and Ritchie (1999) found, however, that in their numerical simulations of hurricanes in unidirectional vertical shear the downshear cold potential temperature anomaly produced via adiabatic mechanisms was eradicated in regions where layers were lifted to saturation. The contribution to upward vertical motion from vortex flow on the distorted isentropes of the tilted vortex was then eliminated. The emergence of a downshear-left convective asymmetry was hypothesized to result from low-level convergence through the downward projection of the downshear-displaced upper-level vortex PV at the surface. Olivia’s tilt with height, while generally from west to east, shows an anticyclonic curvature consistent with the anticyclonic rotation of the shear vector with height. The surface projection of Olivia’s tilted PV at different upper levels could force more broadly distributed mesoscale convection on the downshear side of the vortex, as observed. Although the relative roles of the mechanisms described above are unclear in this case, the involvement of vertical shear in producing the convective asymmetry is likely.

Understanding the influence of vortex-scale dynamics on the distribution of convection in the hurricane inner core should aid in the prediction of the gross precipitation structure of a hurricane as it enters or is embedded in different environmental flows. A clear relationship exists between the mesoscale asymmetry in convection believed to be forced by the vertical shear of the environmental winds (Fig. 10) and the asymmetric pattern of reflectivity (Fig. 2). The largest values of reflectivity occur immediately downwind of the regions of enhanced convection, consistent with hydrometeors being carried up by the updrafts of the convective cells and simultaneously swept downwind by the much stronger primary circulation.

5. Vorticity dynamics

The evolution of Olivia’s symmetric vorticity derived from the dual-Doppler winds at 3-km height is shown in Fig. 11a. Consistent with the vortex weakening discussed in section 3 is a decrease in the radial vorticity

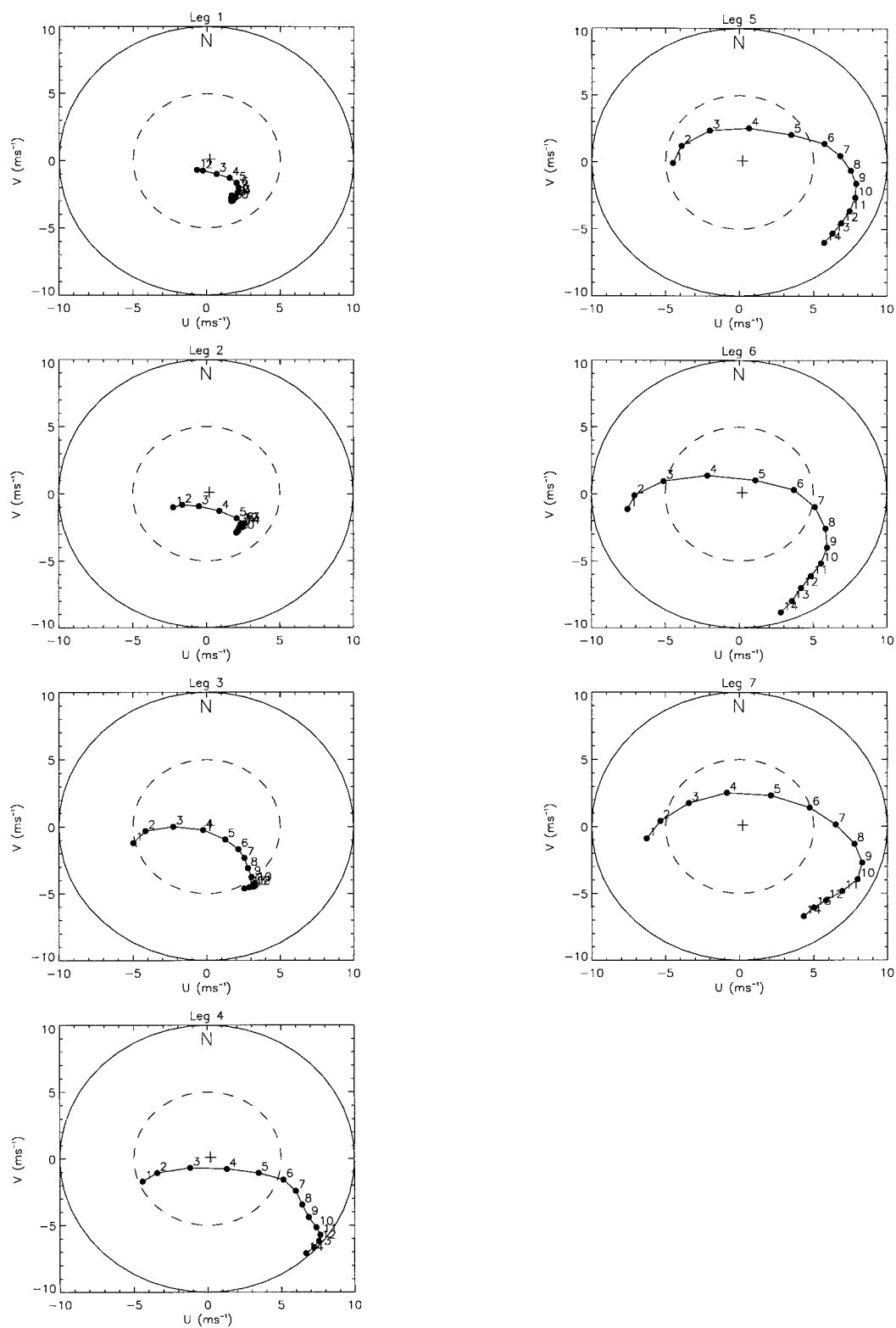


FIG. 8. Hodographs of the area-averaged storm-relative wind ($\mathbf{V}_e - \mathbf{V}_s$) from 0.75- to 10.5-km height for each flight leg. The vertical distance between points is 0.75 km.

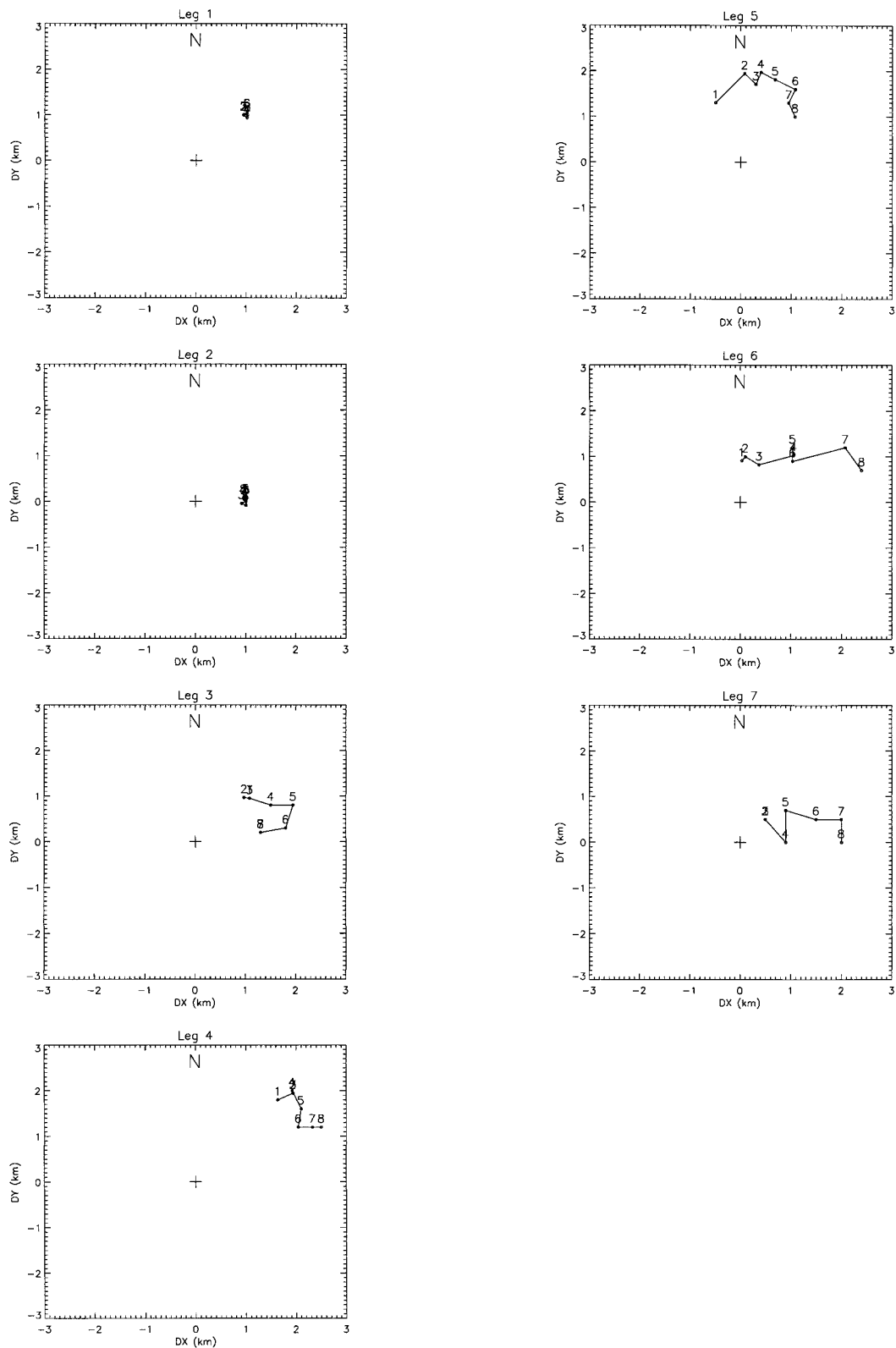


FIG. 9. Departures of the simplex-algorithm center (●) from the flight-level center (+) as a function of height from 0.75 to 6 km for each flight leg.

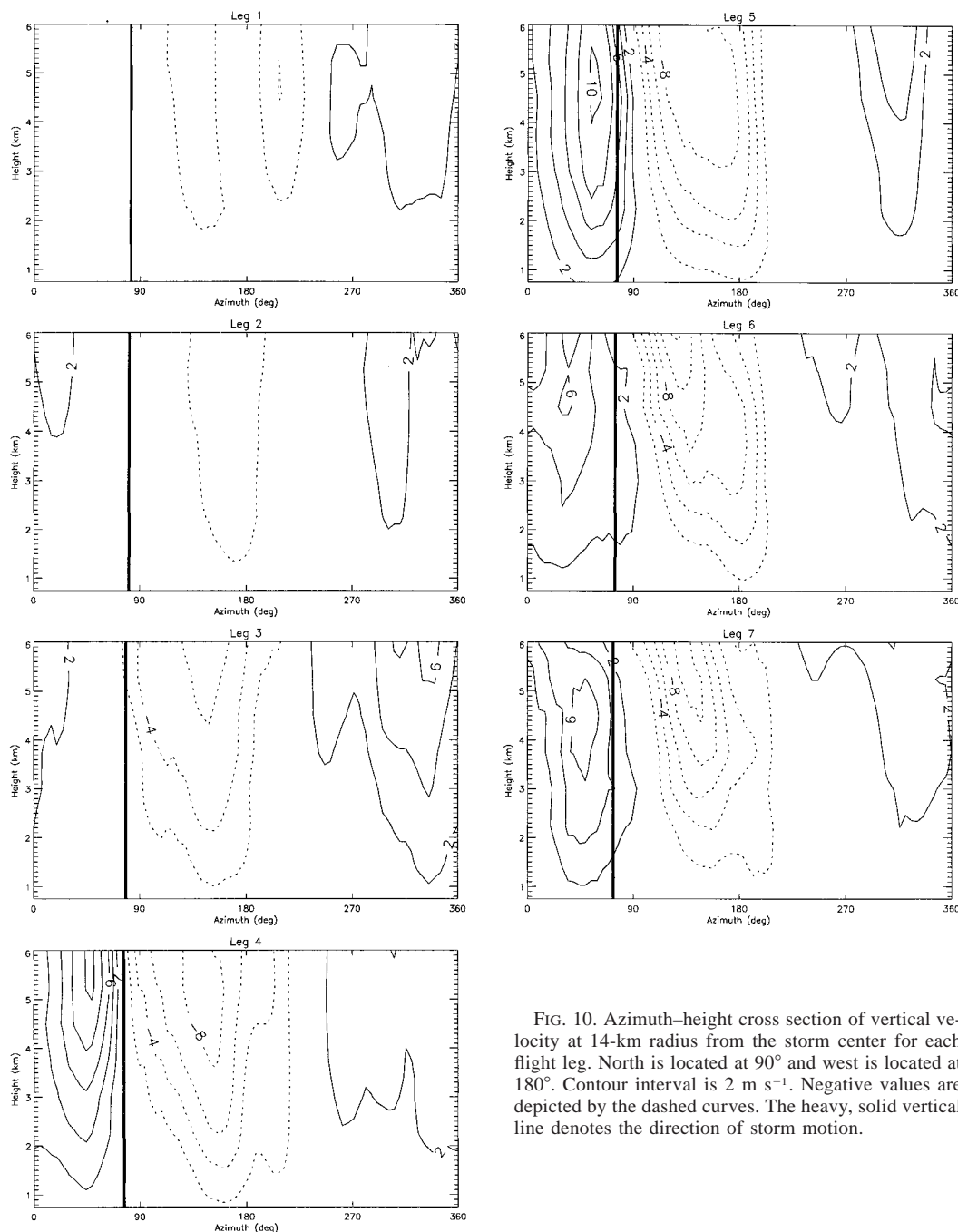


FIG. 10. Azimuth–height cross section of vertical velocity at 14-km radius from the storm center for each flight leg. North is located at 90° and west is located at 180° . Contour interval is 2 m s^{-1} . Negative values are depicted by the dashed curves. The heavy, solid vertical line denotes the direction of storm motion.

gradient near the RMW, most pronounced between legs 3 and 5. One explanation for this gradient reduction is the symmetric divergence (convergence) of absolute vorticity inside (outside) $\sim 12 \text{ km}$ radius. Such changes to the symmetric vorticity profile can also occur through asymmetric mechanisms. The vortex spindown ideas discussed in section 3 may only be a partial explanation for the observed symmetric evolution. For example, the interaction of convectively forced vortex Rossby waves

with the mean flow will lead to changes in the mean vorticity profile (MK; Montgomery and Enagonio 1998; Möller and Montgomery 1999b). Nonlinear mixing of vorticity through the barotropic instability mechanism discussed by S99 will also erode sharp radial gradients of symmetric vorticity.

The details of the internal asymmetric mechanisms are dependent upon the symmetric structure of the vortex. Consider a vortex with monotonically decreasing

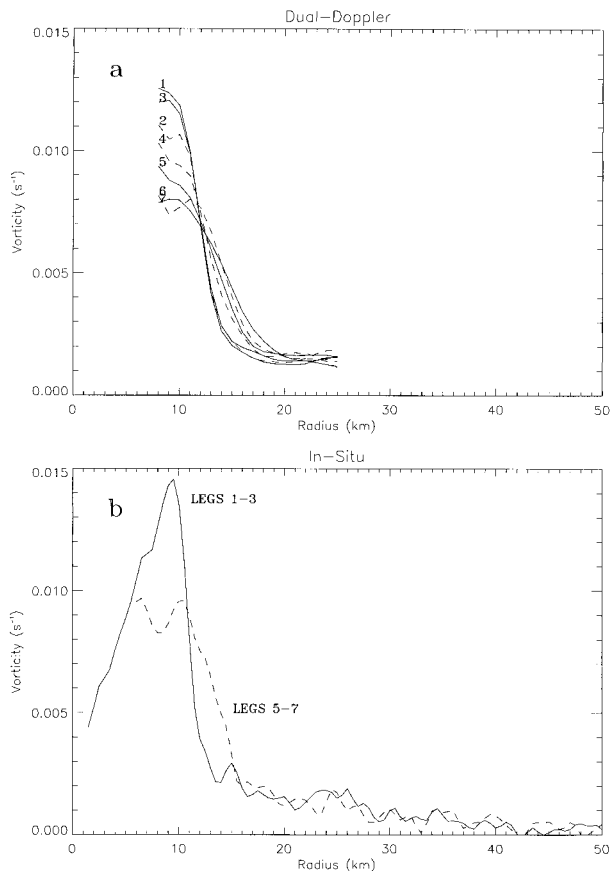


FIG. 11. Symmetric vorticity (s^{-1}) profiles at 3-km height (a) derived from the dual-Doppler analysis (legs 1–7) and (b) computed from aircraft wind measurements averaged over the first three legs (1–3) and last three legs (5–7).

vorticity with radius. This flow satisfies Rayleigh's sufficient condition for exponential stability, prohibiting the mixing mechanism of S99. Vorticity redistribution through vortex Rossby waves can still occur. The Rossby wave phase and group velocities, and the location of wave-mean interaction for such a stable vortex will depend on both the symmetric shear and vorticity profiles. In the case where a reversal in the sign of the vorticity gradient is present and exponential instability is possible, the mean vorticity structure will determine which azimuthal wavenumbers are unstable and their growth rates. Thus, in considering the asymmetric dynamics of Olivia's inner core, it proves useful to first examine the symmetric vorticity structure.

a. Olivia's symmetric vorticity structure

The lack of scatterers within the eye prohibits us from obtaining the complete symmetric vorticity profile in Olivia's inner core using dual-Doppler data alone. If the aircraft wind measurements at 3-km height are averaged over a sufficient number of flight legs through the storm, a proxy for the azimuthal-mean vorticity within the eye

can be computed (Fig. 11b). Averaging the six radials through Olivia during legs 1–3, we find that the radial profile of vorticity takes the form of a ring, with maximum values around 9.5-km radius. A similar analysis for legs 5–7 shows a weaker vorticity gradient near the RMW as depicted in Fig. 11a. Also observed is a broader region of maximum vorticity inside 10 km with values reduced from earlier legs. The lack of flight-level data inside 6-km radius during legs 5 and 6 precludes an extension of the profile to the vortex center. The vorticity profile derived solely from leg 7 data suggests a small depression of the vorticity down to about $8 \times 10^{-3} \text{ s}^{-1}$ (not shown). This evolution of the symmetric vorticity resembles that presented in S99 for a hurricane-like vorticity ring perturbed by an initial broadband vorticity asymmetry. They predicted that some of the high vorticity of the ring is ultimately mixed into the center of the hurricane vortex, forming a monotonic symmetric vorticity profile. High vorticity is also ejected outward in the form of vortex Rossby waves. We will revisit these observations and ideas in section 5c when considering the source of Olivia's vorticity asymmetry. A more comprehensive study of the evolution of symmetric vorticity derived from flight-level data for a number of different storms is currently under way (J. Kossin and M. Eastin 1999, personal communication).¹

b. Olivia's asymmetric vorticity structure

Figure 12 shows the azimuthal variance of vorticity averaged over the 3.5-h observation period. Above 3-km height most of the variance is explained by wavenumber 1. We should note that the magnitude and, to some extent, the structure of wavenumber 1 in vorticity is sensitive to the vortex center definition at each level. Wavenumber 2, which accounts for most of the variance below 3-km height, is fairly robust under changes to the vortex center identification. Higher wavenumbers show a smaller contribution to the total variance, but this may be *in part* a consequence of the aliasing that occurs during the sampling of the inner core. Ideally, one would like actual snapshots of the wind field at each level. The TA radar, however, scans perpendicular to the flight track, requiring planes to fly through the inner core in order to obtain a horizontal wind composite. Parcels of air moving with the tangential winds at the RMW will go through about 90° during the time it takes to composite the inner 15 km of the storm. Therefore, some of the energy contained in the higher wavenumbers will be projected onto lower wavenumbers. While wavenumbers 1 and 2 will be modified by aliasing, simple dynamical ideas to be discussed below do support their observed dominance.

Examination of the perturbation vorticity at 3-km

¹ See note added in proof on page 1678.

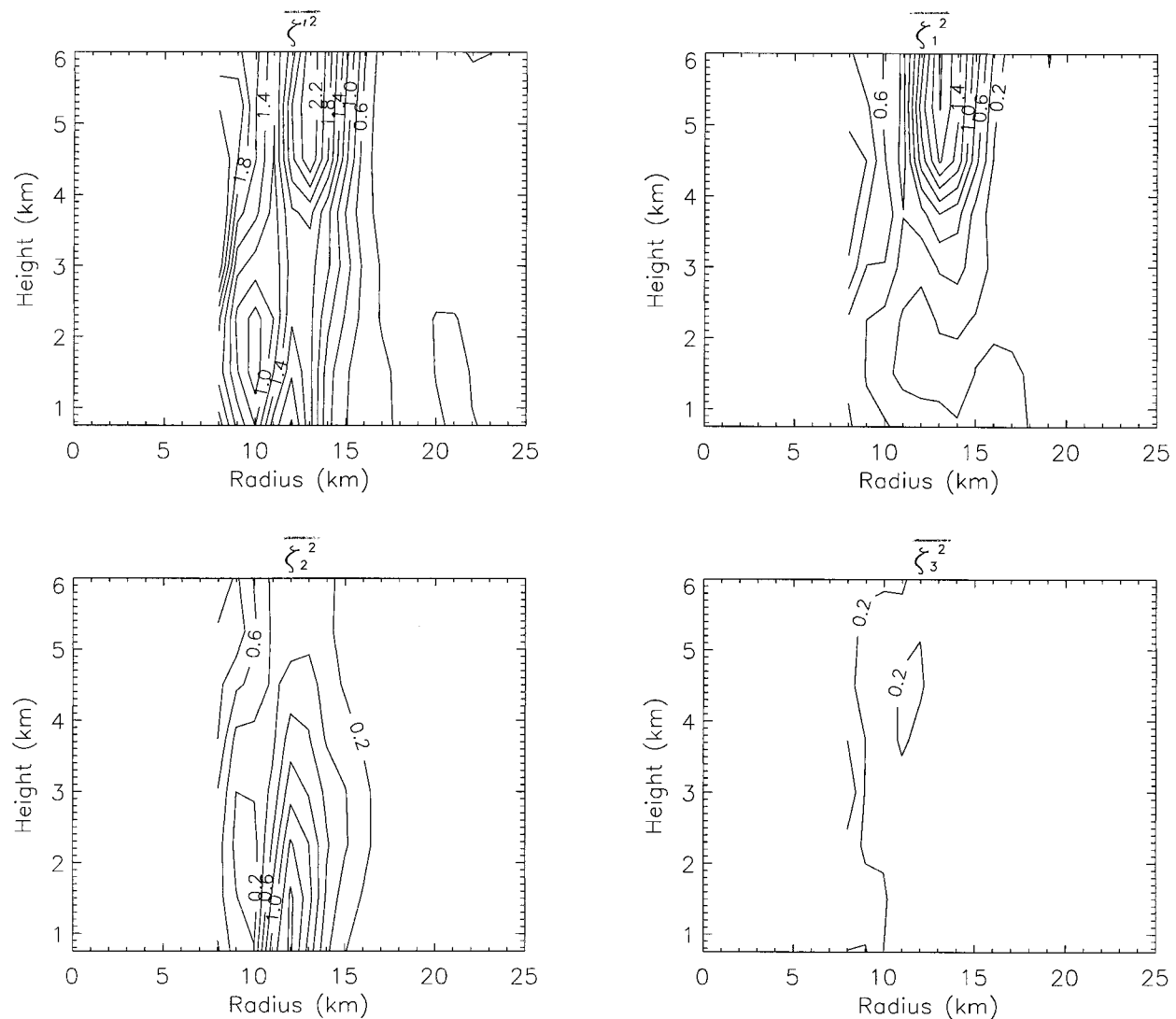


FIG. 12. Radius–height structure of the azimuthal variance of vorticity averaged over the period 2027–2355 UTC. Also shown are the individual wavenumber contributions (1–3) to the azimuthal variance (i.e., wavenumber components of vorticity squared and azimuthally averaged). Contour interval is $0.2 \times 10^{-6} \text{ s}^{-2}$.

height in Fig. 13 shows spiral bands of vorticity with radial wavelengths on the order of 5–10 km located radially outside the regions of high vorticity associated with the above-mentioned wavenumber 2 asymmetry. They are *persistently* located near 20-km radius during the first three legs and then slightly outside this radius during the final legs. The maximum vorticity of the bands ranges from 0.5×10^{-3} to $1 \times 10^{-3} \text{ s}^{-1}$. The bands may be symmetrizing vortex Rossby waves, predicted by MK to occur in the hurricane near core. If so, this is the first observational evidence of such features in the hurricane wind field. One source for the bands may be the symmetrization of the large wavenumber 2 vorticity perturbation near 12-km radius.

We also note the persistent bands of elevated reflectivity in the vicinity of the vorticity bands (see Fig. 2).

Enhanced convection could be triggered by the asymmetric transverse circulation generated in response to momentum flux convergences associated with the vorticity bands. Inner-core spiral bands of reflectivity over open ocean have also been observed by Gall et al. (1998) using ground-based radar. They speculated that the features were similar to boundary layer rolls (Fung 1977), but had insufficient data to make definitive statements about their origin. As discussed in section 1, understanding the role of vortex Rossby waves in tropical cyclone structure and intensity change is an important motivation for this work. The possibility that this data may lend itself to the resolution of finescale spiral vortex Rossby waves is encouraging.

The azimuthal structure of perturbation vorticity at 12-km radius is shown in Fig. 14. Maximum values of

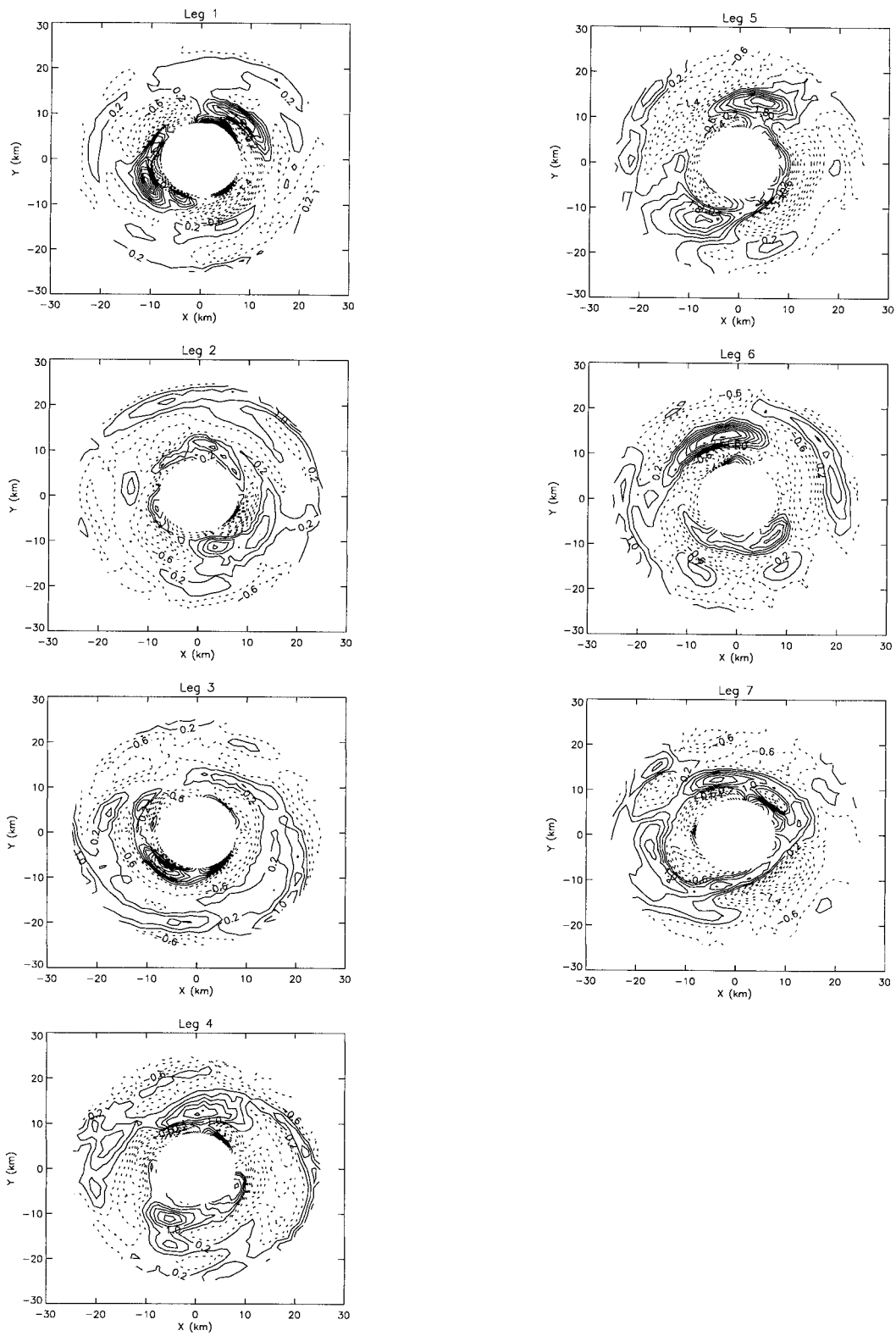


FIG. 13. Perturbation vorticity at 3-km height for each flight leg. Contour interval is $0.4 \times 10^{-3} \text{ s}^{-1}$. Negative values are depicted by the dashed curves.

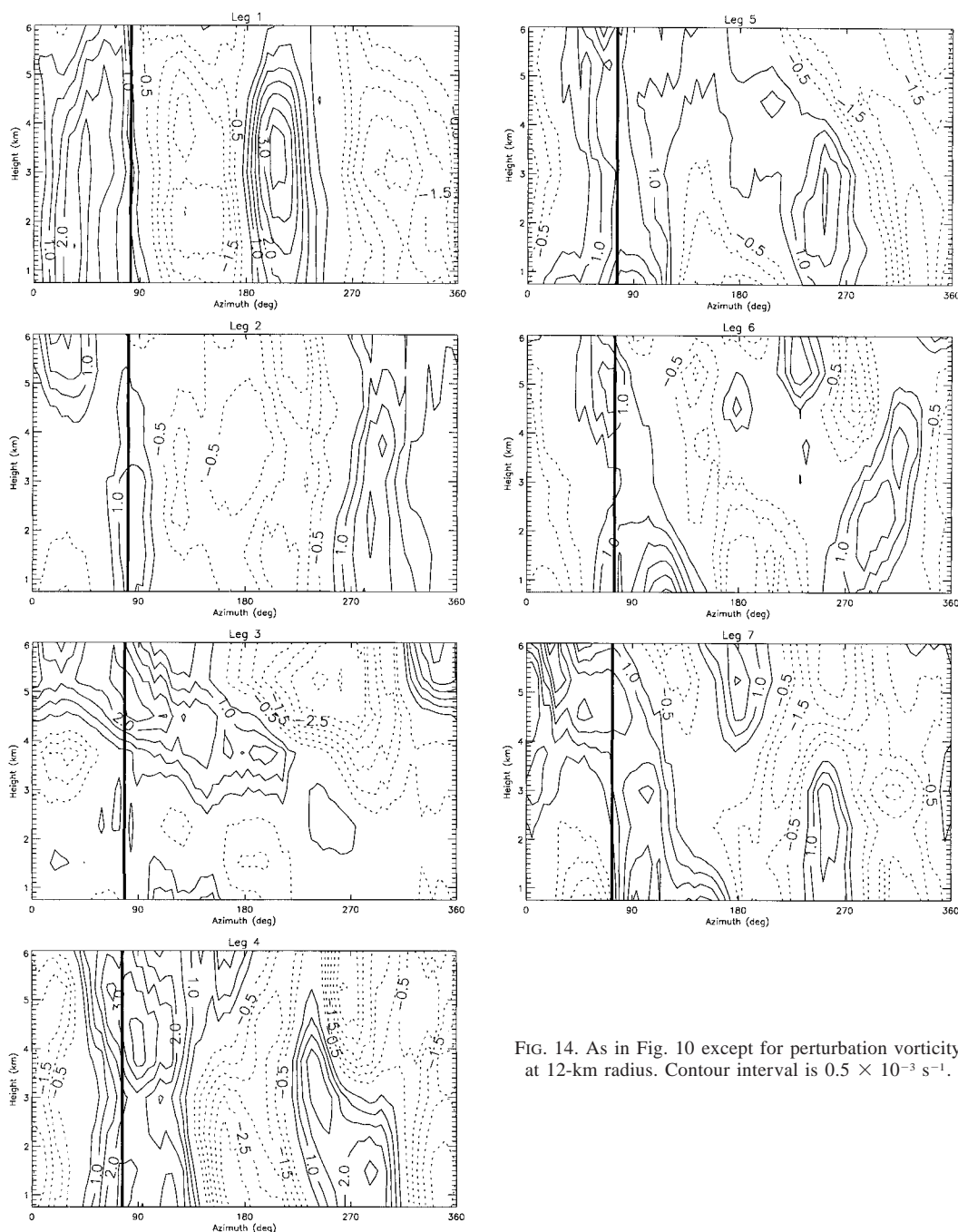


FIG. 14. As in Fig. 10 except for perturbation vorticity at 12-km radius. Contour interval is $0.5 \times 10^{-3} \text{ s}^{-1}$.

positive vorticity are approximately 3×10^{-3} to $4 \times 10^{-3} \text{ s}^{-1}$. During legs 1 and 2, when the symmetric vortex from low to midlevels is nearly barotropic, the vorticity asymmetry tilts little in the azimuth with height. A clear azimuthal wavenumber 2 pattern exists at all heights within the domain during leg 1 and only below 3 km during leg 2. As the vertical shear, vortex tilt, and baroclinicity of the symmetric vortex increase, the azimuthal tilt becomes more pronounced. It is also

observed following leg 2 that the vorticity in the northern quadrant above 3-km height is persistently large and appears to join with an equally large perturbation just above, and extending down into, the boundary layer of Olivia. During legs 4–7 a second positive vorticity asymmetry is observed in the southern quadrant of the storm, although it appears to extend up from low levels and does not reach much above 4-km height. This accounts for the dominance of wavenumber 2 at low levels

and the transition to wavenumber 1 at middle levels observed in Fig. 12.

The evolution of the wavenumber 2 component of vorticity at low levels is shown in Fig. 15. Since the phase and radial location of the wavenumber 2 asymmetry are nearly constant with height below 3 km, we have vertically averaged the vorticity at low levels to provide a bulk estimate of the amplitude. Approximately 20 min separates the end of one composite and the beginning of the next. A parcel of air being advected by the tangential winds at the RMW will make almost an entire orbit around the storm during this time period. The wavenumber 2 vorticity asymmetry may not move with the advective speed, making time continuity difficult to discern simply by looking at consecutive composites.

Following Kuo et al. (1999) we use high temporal resolution radar reflectivity composites to provide an indication of the “instantaneous” tangential speed of this wavenumber 2 feature. In their study of Typhoon Herb (1996) using reflectivity from a Weather Surveillance Radar 1988-Doppler, Kuo et al. found an approximately elliptical eye rotating cyclonically with a period of 144 min. They hypothesized that the eye rotation observed in the reflectivity might be related to the propagation of a wavenumber 2 vortex-Rossby edge wave. According to the linear wave theory of Kelvin (Lamb 1932), the phase speed of a vortex-Rossby edge wave propagating on the vorticity discontinuity of a Rankine vortex is given by

$$c_p = v_{\max} \left(1 - \frac{1}{n} \right), \quad (9)$$

where v_{\max} is the maximum tangential wind speed and n the azimuthal wavenumber. Thus, for wavenumber 2 the propagation speed is one-half v_{\max} . Relating the observed elliptical eye rotation period in the reflectivity field to the propagation period for a vortex Rossby wave, Kuo et al. found that (9) was approximately valid. It should also be noted that the nonlinear Kirchhoff solution for elliptical eye rotation (Lamb 1932) agrees well with the above linear solution as long as the ratio of minor to major axis is close to one. Figure 16 shows the LF reflectivity evolution of Hurricane Olivia's inner core at 3-km height during the period spanned by leg 5. As in the case of Typhoon Herb, the eye appears elliptical and rotates cyclonically in time. The ratio of minor to major axis is approximately 0.7. Over the 7-min period the eye rotates through about 50°. The eye rotation period is then estimated to be 50 min. From the wind analysis during this time the RMW and maximum tangential wind speed at 3-km height are 14 km and 57 m s⁻¹, respectively. The circulation period for a parcel being advected around the vortex at the RMW is then 25 min, or one-half the eye rotation period, as predicted by (9).

Supplementing the reflectivity with the wind field data allows this hypothesis linking the rotation of the

reflectivity ellipse to the rotation of the associated vorticity asymmetry to be examined further. The orientation of the reflectivity ellipse observed in Fig. 16 is consistent with the phase of the wavenumber 2 component of vorticity shown in Fig. 15 for leg 5; that is, the positive vorticity asymmetry lies along the major axis. An attempt to extend this interpretation to other times by comparing the observed phase evolution to that predicted by (9) was met with limited success. Only between legs 5 and 6 did the phase of wavenumber 2 evolve in a manner consistent with a vortex-Rossby edge wave. In addition to aliasing issues, discrepancies between observations and the linear theory described by (9) may be attributed to physical complications heretofore neglected.

The basic state vorticity shown in Fig. 11 is not Rankine. Although the radial gradient of mean vorticity outside the RMW is quite steep, discrepancies between Kelvin's edge wave solution and the wave solution on a continuous vorticity profile are expected. In the inviscid limit the vorticity waves described by (9) propagate indefinitely around the vortex as discrete normal modes that never axisymmetrize. When the gradient of vorticity is no longer confined to a single radius (but the profile remains monotonic), axisymmetrization of the initial vorticity asymmetry is expected for all azimuthal wavenumbers in the *linear* problem (Sutyrin 1989; Carr and Williams 1989; Smith and Montgomery 1995; MK). The axisymmetrization mechanism also affects the phase propagation such that as the central radial wavenumber increases due to the shearing by the basic-state flow, the azimuthal phase speed of the Rossby waves approaches the local tangential wind speed (MK).

The influence of cumulus convection on the Rossby wave propagation must inevitably be considered. The extension of the two-dimensional barotropic *local* dispersion relation for vortex Rossby waves derived by MK to a stably stratified barotropic circular vortex in gradient balance is given by (Möller and Montgomery 1999a)

$$\omega = n\bar{\Omega}_0 + \frac{n\bar{\xi}_0}{R\bar{q}_0} \frac{\bar{q}'_0(r)}{[k^2 + n^2/R^2 + (\bar{\eta}_0\bar{\xi}_0 m^2)/N^2]}, \quad (10)$$

where n , k , and m are the azimuthal, radial, and vertical wavenumbers, respectively; R the reference radius (see MK); \bar{q}'_0 the radial derivative of the barotropic basic-state PV; $\bar{\eta}_0$ the absolute vorticity; $\bar{\xi}_0$ the inertia parameter; and $\bar{\Omega}_0$ the angular velocity. In regions of convection the static stability, and thus N^2 , will be reduced from that in the nonconvective regions, so the phase propagation of the waves will be modified. According to (10), the decrease in Rossby deformation radius in the convective regions will reduce the retrograde propagation of vortex Rossby waves. The precise dependence of vortex Rossby wave propagation on static stability could be explored with a high spatiotemporal res-

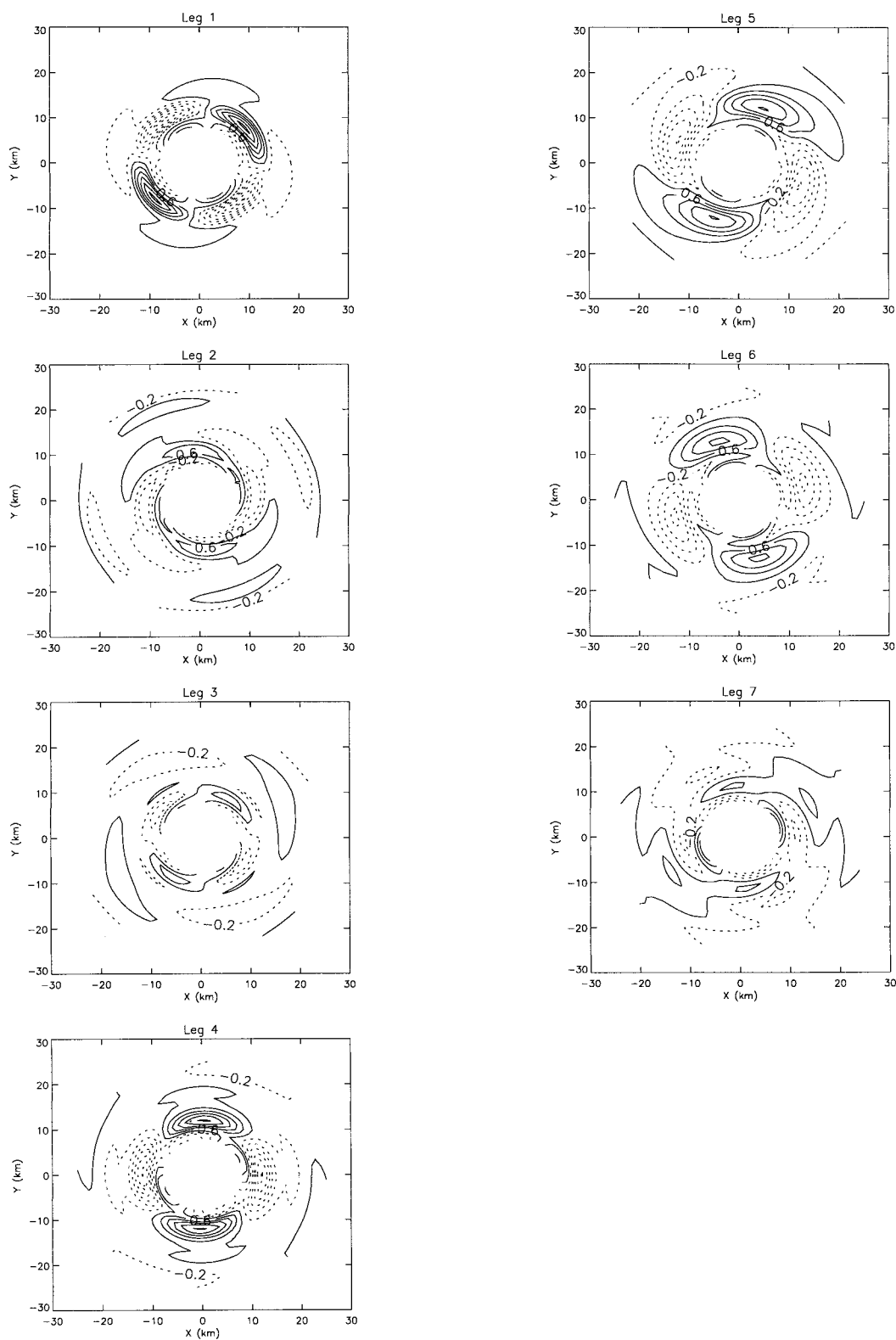


FIG. 15. Azimuthal wavenumber 2 component of vorticity vertically averaged over the lowest 3 km for each flight leg. Contour interval is $0.4 \times 10^{-3} \text{ s}^{-1}$. Negative values are depicted by the dashed curves.

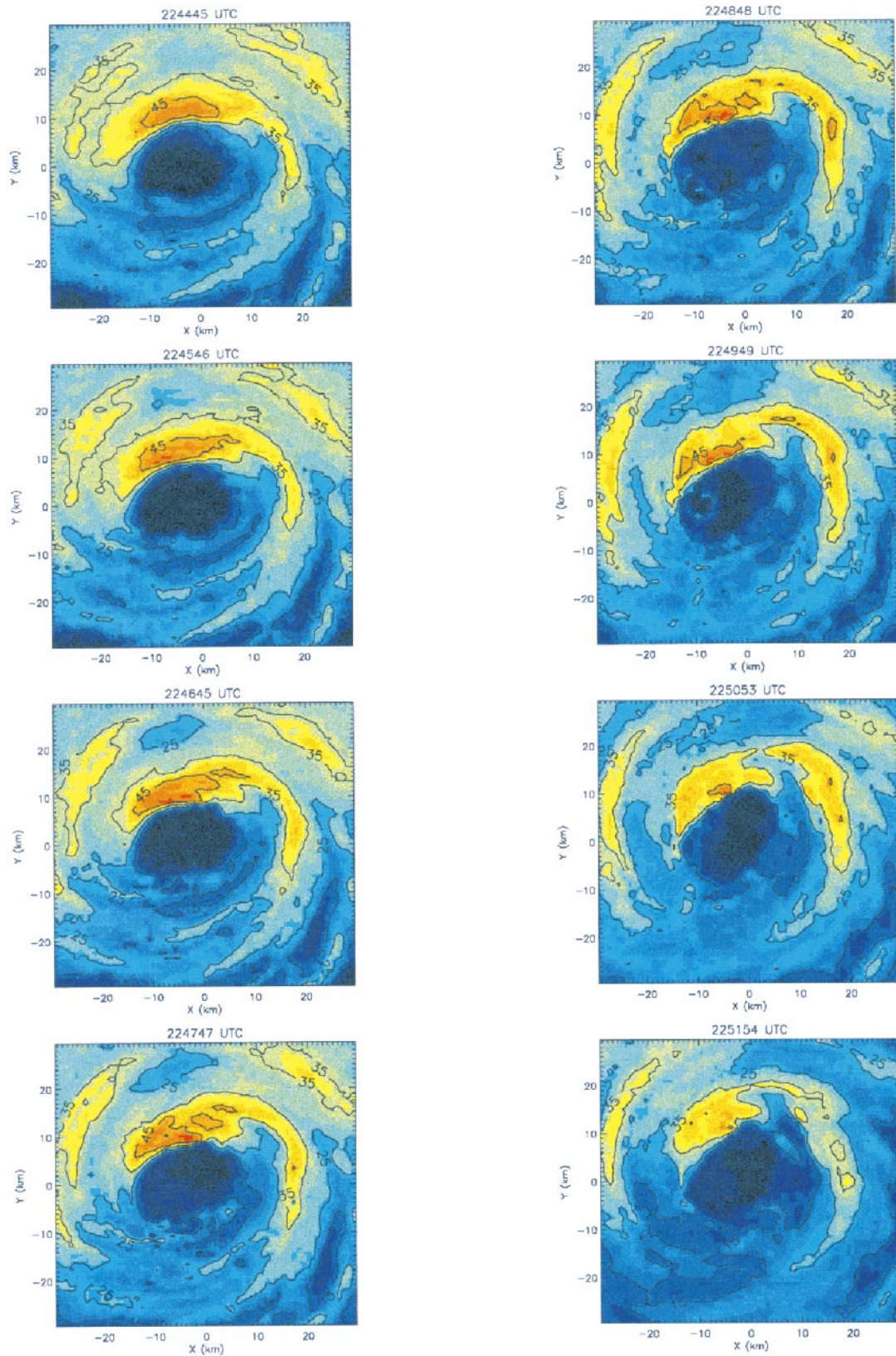


FIG. 16. Olivia inner-core LF reflectivity composites at 3-km height. Period spanned is 2244–2251 UTC at 1-min time intervals. Contour interval is 10 dBZ.

olution dataset generated by a full-physics numerical model.

We conclude that over the time interval defined by leg 5 (and perhaps leg 6) the wavenumber 2 asymmetry in vorticity propagates in a manner consistent with a vortex-Rossby wave packet of near-discrete structure. Although symmetrization and convection will modify its propagation speed, the greatest obstacle to extending this interpretation to other observation times is the 30-min time resolution of the dual-Doppler wind data. The hypothesized propagation period of the vorticity asymmetry is approximately 50 min. Thus, to shed further light on the propagation characteristics, snapshots of the wind field would be required about every 10 min. Insight into the *source* of the wavenumber 2 vorticity asymmetry may still be obtained by examining the observations in the context of recent numerical and theoretical studies of vortex dynamics.

c. Sources of vorticity asymmetry

1) CONVECTIVE AND ENVIRONMENTAL SOURCES

Asymmetric convection in the eyewall is expected to produce asymmetries in PV. The gradient of the diabatic heating rate associated with convection projected onto the absolute vorticity vector tends to be positive at low levels and negative at high levels. Thus, according to the PV equation, a positive (negative) anomaly is produced at low (high) levels (Haynes and McIntyre 1987). Convection in the eyewall will project onto a number of azimuthal wavenumbers, but it is not apparent from observations of Olivia's vertical velocity and reflectivity structures that wavenumber 2 is being preferred. Nevertheless, convective asymmetries will play an important role in the internal vorticity dynamics to be discussed below by providing an initial broadband vorticity perturbation to the symmetric vortex.

The interaction of Hurricane Olivia with the large-scale deformation field could have excited the near-core wavenumber 2 asymmetry in vorticity (e.g., Glatz and Smith 1996). Another facet of the vortex-environment interaction is the vertical shearing of the hurricane, as discussed in section 4. The downward projection of the upper-level PV of the tilted vortex on the low-level vortex PV results in vorticity asymmetry at low levels. Wavenumber 1 will dominate the asymmetry in the case of unidirectional shear. In section 4 we noted that higher wavenumbers may become increasingly important if the direction of vortex tilt varies with height as in the case of Hurricane Olivia. This vertical shear mechanism could be activated following leg 3, when the local vertical shear increases, but seems an unlikely candidate for the production of the wavenumber 2 asymmetry observed during leg 1. At that time the vortex shows little tilt with height.

The enhanced convection on the east side of Olivia argued in section 4 to be triggered by increased vertical

shear following leg 2 is generally flanked radially inward by strong downdrafts. Gamache et al. (1997) suggested that perturbation vorticity may be produced in such regions via the tilting of radial vorticity filaments by the radially sheared vertical winds (e.g., in the front right quadrants of Figs. 10 and 13 during leg 5). The positive vorticity in the front quadrant of Olivia following leg 2 near 12-km radius *could* have resulted from such a mechanism, leading to the persistent wavenumber 1 in vorticity above 3-km height. One could alternatively make the argument that preexisting vertical vorticity associated with the vorticity asymmetry in the southern quadrant during leg 2 was vertically and azimuthally advected. Stretching of this vorticity in the region of strong updrafts in the eastern quadrant could have then resulted in the midlevel vorticity asymmetry observed during leg 3. Both mechanisms, while plausible, mainly shed light on the origin of the wavenumber 1 vorticity asymmetry observed above 3-km height.

2) INTERNAL DYNAMICS: AN ANALOG MODEL

We now consider the possibility that the production of the dominant wavenumber 2 asymmetry in vorticity at low levels is directly tied to the inner-core symmetric vortex profile of Olivia. To elucidate the dynamical mechanisms we utilize the nondivergent barotropic vorticity equation in a series of four numerical experiments. A semispectral model was used to perform the simulations. A discussion of the pertinent model details is provided in appendix B of Montgomery and Enagonio (1998). The radial grid spacing used here is 0.5 km and the number of radial points is 200. The azimuthal truncation is 16 modes.

Figure 17 shows the initial vorticity profiles used in each of the four cases. The profiles are based on Olivia's observed symmetric vorticity shown in Fig. 11 with some modifications. Although the aircraft measurements suggest a ring profile of vorticity, we first consider the case where the vorticity inside the eye is well mixed as in a modified Rankine vortex (cases A and B). We then examine the asymmetric dynamics of an elevated vorticity ring (cases C and D) as discussed in S99. In cases A–C the profile of dual-Doppler derived tangential wind outside 18-km radius was replaced by an $r^{-0.4}$ fit to the flight-level observations. In case D we consider the effect of the “bump” in symmetric vorticity observed near 25-km radius during legs 1 and 2 on the asymmetric evolution of the flow. All of the above vortices were perturbed with an initial pulse of cyclonic vorticity centered at 12-km radius and radially aligned:

$$\zeta' = \zeta'_{\max} e^{-(r'/r_d)^2}, \quad (11)$$

where $\zeta'_{\max} = 0.1 \bar{\zeta}_{\text{RMW}}$, $r_d = 5$ km, and r' is the radius from the asymmetry center.

Cases A and B demonstrate the dependence of the asymmetric vorticity evolution on the slope of the mean vorticity gradient in the vicinity of the RMW. Solid-

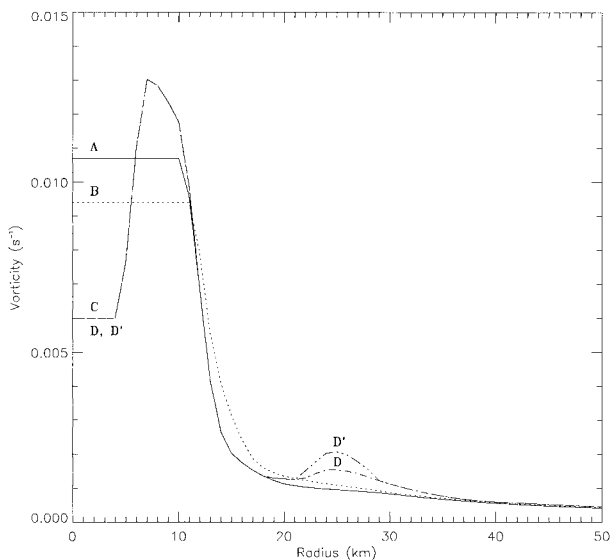


FIG. 17. Initial profiles of symmetric vorticity (s^{-1}) used in the nondivergent, barotropic numerical simulations. Shown are cases A (solid), B (short dash), C (long dash), D (dash-dot), and D' (dash-dot-dot-dot).

body rotation is assumed inside the RMW in both cases, but the larger radial vorticity gradient of case A reflects the observations of leg 1 and the weaker gradient of case B the observations of leg 4. In cases A and B the vortex is exponentially stable for all azimuthal wavenumbers (Gent and McWilliams 1986). The linear dynamics is then governed exclusively by the continuous spectrum of sheared vortex-Rossby wave disturbances (Smith and Montgomery 1995; MK). The linear evolution of the vorticity perturbation (11) appears similar in both cases, taking the form of vortex-Rossby wave trailing spirals (not shown). This is in contrast to the observations in Fig. 13 that, for many of the flight legs, show a more modal (i.e., nonchanging) structure to the vorticity asymmetry. When the profiles for cases A and B are instead perturbed with a pure wavenumber 2 asymmetry, a noticeable distinction between the initial linear evolutions is evident. The steeper profile supports vortex Rossby waves, which initially look modal in structure like the waves predicted by Kelvin's solution (Fig. 18a). The estimated propagation period for the wave (~ 35 min) agrees with (9). The profile with the radially broader transition region from high to low vorticity supports more tightly wound vortex Rossby waves (Fig. 18b). Although the anticyclonic horizontal shear is less in this case, the Rossby elasticity is also less. The net result is a greater tendency for sheared, trailing spiral disturbances. In both cases the wavenumber 2 vorticity asymmetry ultimately decays as axisymmetrization proceeds. This distinction in wave structures for cases A and B is not readily apparent in the observations shown in Fig. 15. We also note that these profiles, while they may allow azimuthal propagation of wavenumber

2, do not prefer the emergence of wavenumber 2 over other wavenumbers.

The next two profiles (C and D) highlight the potential importance of barotropic exponential instability in the generation of asymmetric vorticity in the near-core region, and more specifically a mechanism preferring the emergence of wavenumber 2. [Algebraic instabilities associated with wavenumber 1 may also be playing a role in the asymmetric evolution of Olivia (Smith and Rosenbluth 1990).] Both profiles C and D satisfy Rayleigh's necessary condition for barotropic instability (Gent and McWilliams 1986). To determine whether the profiles indeed support linearly unstable modes, we performed an inviscid, nondivergent eigenanalysis of the continuous problem (see appendix B). Nonlinear simulations in which the mean profiles were perturbed by (11) have been carried out and are summarized in order to convey the effects of nonlinearities on the asymmetric vorticity evolution.

The ring profile of case C is exponentially unstable for wavenumbers 2 through 4, with wavenumber 2 being the most unstable. All other wavenumbers are exponentially stable. The e -folding time for wavenumber 2 is 45 min. Changes in the width of the vorticity ring or the ratio of the maximum vorticity to the vorticity at the vortex center will alter the growth rate (S99). Keeping in mind that Olivia's actual vorticity profile may depart from the observations shown in Fig. 11, this value of the e -folding time is therefore intended as a reasonable estimate of the actual growth rate.

The nonlinear simulation in which the case C profile is perturbed by (11) shows the emergence of the unstable wavenumber 2 modal structure in the vicinity of the RMW after a few e -folding times (Fig. 18c). Elevated vorticity from the ring mixes into the vortex center after 4–5 h, resulting in a vortex profile with maximum symmetric vorticity at the center. The transition of Olivia's symmetric vorticity from a well-defined ring to a near-monotonic profile, or at least a broader ring, resembles this simulated evolution. It is plausible that the weakening of symmetric eyewall convection in Olivia inferred from Fig. 2 reduced the symmetric PV generation in the eyewall. In the absence of sufficient PV generation to maintain the ring, barotropic instability then set in to stabilize the vortex profile. The wavenumber 2 asymmetry at low levels of Olivia, according to case C, could then be interpreted simply as a by-product of the vorticity mixing process.

The dual-Doppler observations in Fig. 11a indicate a possible secondary vorticity ring around 25-km radius during legs 1 and 2. This bump is incorporated into the profile of case D. Before examining its effect on the inner-core dynamics, we consider first the question of why this bump in vorticity might exist where it does in the first place. The primary ring of vorticity is believed to form through frictional convergence and vortex-tube stretching in association with strong cumulus convection in the eyewall (e.g., Möller and Smith 1994). One

explanation for the secondary bump in vorticity is that vortex Rossby waves excited in the eyewall prior to leg 1 propagated radially outward, stagnating outside the RMW. The nondivergent, barotropic simulations of MK suggest that the subsequent wave-mean interaction produces a decrease in mean relative vorticity in the vicinity of the stagnation radius and an increase in mean relative vorticity radially outward of the stagnation radius. The radial distance between the location of the initial asymmetry and the stagnation radius, derived from (10), is given by

$$\delta r = \frac{\bar{\xi}_0 \bar{q}_0'}{\bar{q}_0 R \bar{\Omega}_0'} \frac{1}{[k_0^2 + n^2/R^2 + (\bar{\eta}_0 \bar{\xi}_0 m^2)/N^2]}, \quad (12)$$

where k_0 is the initial radial wavenumber. Using the two-dimensional nondivergent version of (12) (see MK) evaluated at $R = 12$ km, and assuming an initial central radial wavelength of 5 km (horizontal eyewall scale), the stagnation radius for wavenumber 1 is approximately 25 km from the RMW. The effects of reduced static stability in the convective regions on radial wave propagation and the symmetric radial inflow will reduce this value somewhat.

The impact of the vorticity bump on the asymmetric vorticity evolution may be important, causing deviations from the evolution described for case C. Laboratory experiments involving two-dimensional perturbations to vortices with monotonically increasing vorticity from the RMW to the vortex center and a bump in vorticity outside the RMW (i.e., an associated secondary tangential wind maximum) have been found to produce tripolar vortex structures dominated by wavenumber 2, with a central elliptical region of high vorticity and satellite regions of anticyclonic vorticity along the minor axis of the ellipse (e.g., Kloosterziel and van Heijst 1991). If the vorticity profile satisfies Rayleigh's necessary condition for barotropic instability, one often finds that such stable tripolar vortex structures emerge. Montgomery and Enagonio (1998) were evidently the first to reveal a tripolar vortex in three-dimensional vortex flow at the upper levels of their QG model when a two-cluster convective anomaly was used to perturb an initially barotropic vortex. Kossin et al. (2000, manuscript submitted to *J. Atmos. Sci.*) demonstrated that tripolar vortices can emerge from hurricane-like vortex profiles with a secondary vorticity maximum radially outside the maximum at the vortex center.

Experiments using the modified Rankine profile of case A with the secondary bump of vorticity of case D did not produce a stable tripolar vortex. A barotropic stability analysis of a piecewise-uniform approximation to this profile showed that wavenumber 2 is in fact marginally stable (J. Kossin 1998, personal communication). A stable tripolar vortex was observed to emerge upon increasing the vorticity of the bump by 35%. The question then arises of whether a stable tripolar vortex can emerge when the vorticity is depressed in the central region of

the vortex, as might be expected in the lower- to mid-tropospheric portion of a hurricane (see Fig. 11b).

The vorticity profile for case D' is similar to that of case D, but with the secondary bump in vorticity elevated by 35%. A continuous nondivergent eigenanalysis of this profile found, in addition to the mode described in case C, a second unstable mode for wavenumber 2. This mode is associated with the phase-locking of vortex Rossby waves propagating on the outer edge of the primary ring and the inner edge of the outer bump. Its e -folding time is 85 min, or approximately twice that of the mode associated with the primary vorticity ring. According to linear dynamics, then, the unstable mode observed in case C should emerge first and tend to dominate the solution. Whether this remains true once wave-wave interactions become significant has important implications for the excitation of tripolar vortex structures in the lower-tropospheric region of hurricanes.

The nonlinear simulation in which the case D' profile is perturbed by (11) shows essentially the same evolution of total vorticity as was observed in case C (Fig. 18d). A tripolar vortex structure is not observed to emerge at long times. As long as the growth rate of the unstable mode associated with the primary ring is significantly larger than that of the bump, we find that tripolar vortex structures do not materialize. Thus, based on the simple nonlinear initial-value experiments presented here, the most plausible (barotropic) internal mechanism for producing Olivia's wavenumber 2 asymmetry in vorticity at low levels during the observation period is the barotropic instability of the primary ring of vorticity.

6. Summary and conclusions

Seven consecutive airborne dual-Doppler wind analyses for Hurricane Olivia spanning a 3.5-h period, supplemented with reflectivity and aircraft wind data, permit exploration of the inner-core dynamics of a weakening storm embedded in environmental vertical shear. The true dual-Doppler sampling technique employed reduces the compositing time of the inner core, allowing for greater confidence in the representation of azimuthal wavenumbers 0–2 in the wind field. The purpose of this paper was to provide additional observational justification for studying the role of asymmetric dynamics in hurricane structure and intensity change, and to determine to what extent the data can be used to explore recent ideas regarding vorticity mixing and axisymmetrization.

For completeness, we first considered the symmetric weakening of Olivia. We did not speculate as to the primary cause of the weakening, but it likely involved both increases in the environmental vertical shear and reductions in the SSTs as Olivia moved northward. The magnitude of the observed near-linear decrease in tangential winds with time in the vicinity of the RMW agreed with the axisymmetric vortex spindown predic-

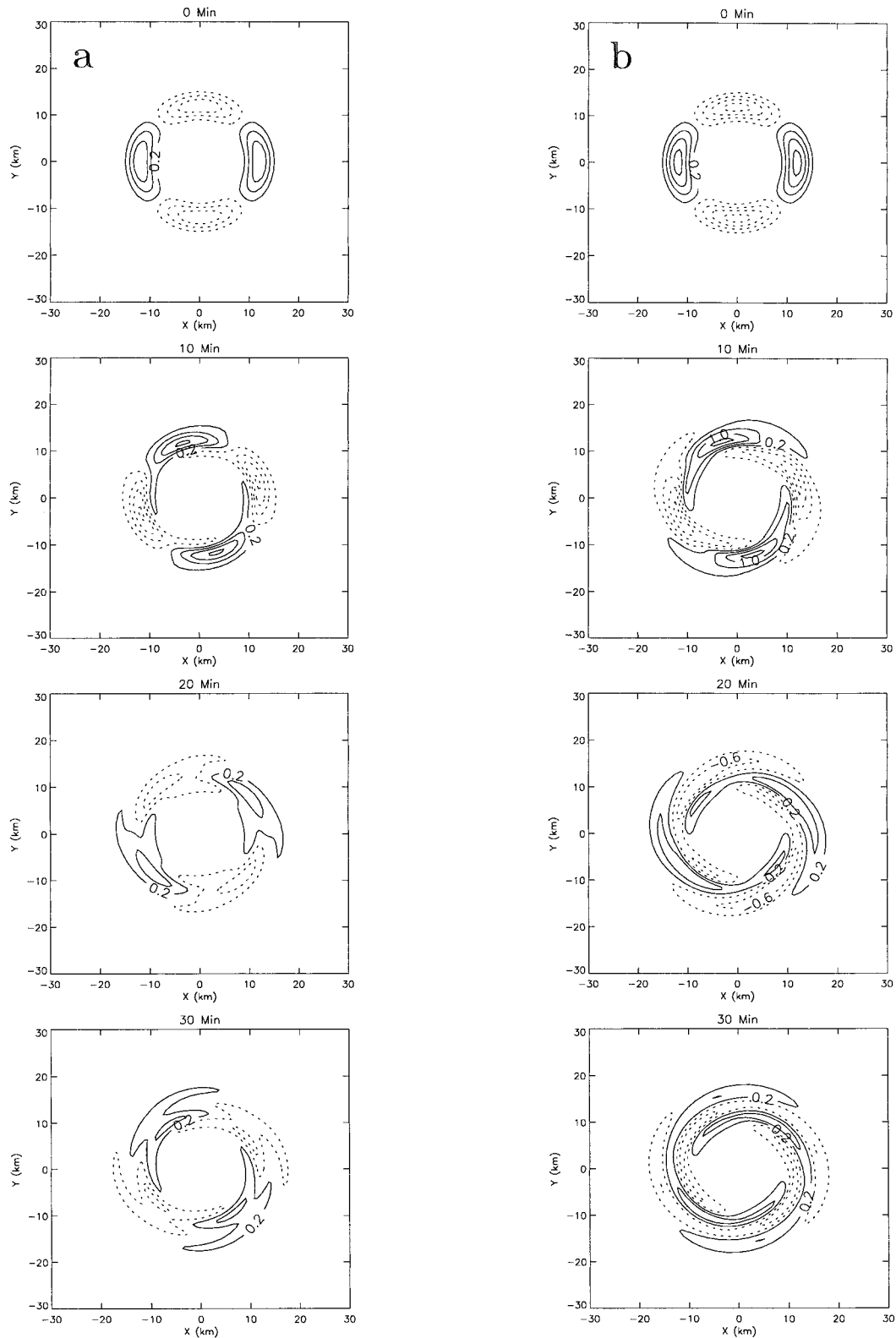


FIG. 18. Numerical simulation of the wavenumber 2 component of vorticity for (a) case A and (b) case B. Contour interval is $0.4 \times 10^{-3} \text{ s}^{-1}$. Initial condition is followed by snapshots of the evolution every 10 min. Negative values are depicted by the dashed curves. Also shown are numerical simulations of the total (mean plus perturbation) vorticity for (c) case C and (d) case D'. Contour interval is $2 \times 10^{-3} \text{ s}^{-1}$. Initial condition is followed by snapshots of the evolution every 2 h, except for the last plot in the sequence, which depicts the well-mixed state at 10 h.

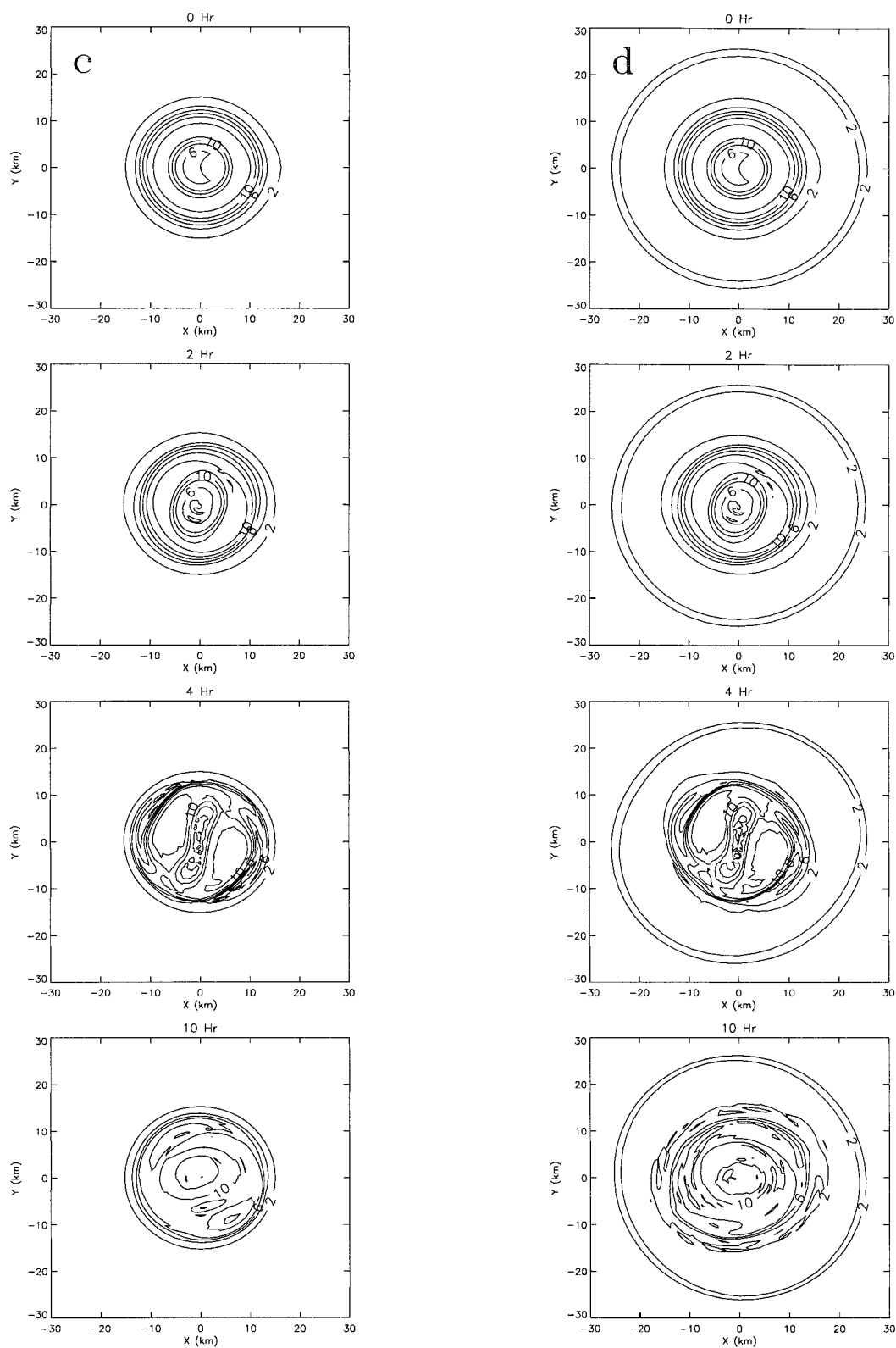


FIG. 18. (Continued)

tions of Eliassen and Lystad (1977) despite the observation of inflow up to 3.5-km height and the presence of environmental vertical shear. Discrepancies between the estimated and symmetric budget tendencies of symmetric tangential wind were not surprising given the oscillatory structure of the transverse flow, suggesting the presence of symmetric inertia-gravity waves. The 30-min time resolution of the dataset does not allow these features to be resolved and removed. The tendency associated with the waves will to some extent mask the actual spindown tendency of the vortex tangential winds. We decided that until issues with the symmetric circulation can be resolved, the contribution of eddy fluxes to the mean tangential momentum budget should not be included. Asymmetric mechanisms, however, appeared to play an important role in the structural evolution of Olivia's inner core.

The increase in westerly local vertical shear from 3–5 to 15 m s^{-1} over the lowest 10-km depth during the 3.5-h observation period was accompanied by an increase in the west to east tilt of the storm center with height and a dramatic increase in convection on the east side of the vortex. A double maximum in the convection was found with largest upward motion downshear left ($\sim 8\text{--}12 \text{ m s}^{-1}$) and weaker upward motion downshear right ($\sim 4\text{--}6 \text{ m s}^{-1}$). These observations are consistent with recent numerical simulations of hurricane-like vortices in vertical shear (Jones 1995; DeMaria 1996; Bender 1997; Frank and Ritchie 1999).

For barotropic vortices tilted by vertical shear with small Rossby numbers we derived an expression for the \mathbf{Q} -vector convergence, illustrating the relative contributions to vertical motion from vortex motion on ambient isentropes and vortex motion on the isentropes of the tilted vortex. This formula was verified to produce qualitatively correct results for Rossby numbers near unity through a comparison with PE simulations performed by Trier et al. (1998). Future work will extend these results to hurricane-strength flows by utilizing the AB generalization of the QG omega equation.

The vorticity asymmetry in the inner core was dominated by an azimuthal wavenumber 2 feature below 3-km height and a wavenumber 1 feature above 3 km, both maximum near the RMW. During leg 1 the wavenumber 2 asymmetry extended from low to middle levels of the storm and appeared to decay through leg 2. An increase in the wavenumber 1 asymmetry at middle levels around leg 3 coincided with the increase in vertical shear. Tilting of horizontal vorticity by enhanced convection on the east side of Olivia, as suggested by Gamache et al. (1997), is a possible mechanism for the production of the wavenumber 1 asymmetry, but an accurate vorticity budget cannot be performed with this data and, thus, no definitive conclusions can be drawn. Following leg 3 a low-level wavenumber 2 asymmetry reemerged and persisted through the end of the observation period.

Lower fuselage reflectivity composites at low levels

during leg 5 depicted an elliptical eye rotation. The rotation period was consistent with Kelvin's predictions for a wavenumber 2 vorticity asymmetry propagating on the discontinuity of a Rankine vortex. The major axis of the reflectivity ellipse was found to be aligned with the axis of positive vorticity of the wavenumber 2 vorticity asymmetry observed during leg 5. Since this asymmetry likely had its structure and azimuthal phase speed modified by convection and axisymmetrization, we did not observe general agreement between the phase evolution from leg to leg and Kelvin's simple dispersion relation, except between legs 5 and 6.

The possibility that the low-level wavenumber 2 asymmetry formed as a result of internal dynamical mechanisms was considered in light of recent theoretical and numerical work by S99 exploring the two-dimensional barotropic instability of hurricane-like vorticity profiles. Olivia's inner-core vorticity profile during leg 1 was found to take the form of a vorticity ring and was most unstable to wavenumber 2 perturbations. The profile during later legs suggested a broader ring of vorticity with increased values at the vortex center and reduced values in the vicinity of the ring peak. This evolution of the symmetric vorticity is consistent with the numerically simulated breakdown of a vorticity ring through barotropic instability described by S99 and our own simulations using Olivia-like profiles. If this interpretation is correct, the wavenumber 2 vorticity asymmetry found in Olivia's eyewall region is an expected by-product of the vorticity ring breakdown.

Part of the vorticity mixing hypothesized to occur in the hurricane near-core region is the expulsion of high vorticity from the eyewall in the form of vortex Rossby waves (MK; S99). The perturbation vorticity at 3-km height (Fig. 13) shows spiral bands of vorticity with radial wavelengths of 5–10 km outside of the regions of high vorticity associated with the wavenumber 2 vorticity asymmetry. These features may be symmetrizing vortex Rossby waves. Spiral bands of enhanced reflectivity were observed in the vicinity of the vorticity bands, suggesting a coupling of the vorticity bands to the boundary layer through a forced asymmetric transverse circulation. The possible connection between these vorticity and reflectivity features is of great interest and is a topic of current study.

Note added in proof: Kossin and Eastin (2000, manuscript submitted to *J. Atmos. Sci.*) have shown that during hurricane intensification the vorticity profile tends to be ringlike. For most cases when the storm is steady or weakening, the vorticity profile becomes more monotonic, consistent with the barotropic instability mechanism of S99 and the observations presented here.

Acknowledgments. This work was supported in part by the Cooperative Institute for Research in the Atmosphere (CIRA) at Colorado State University and from National Science Foundation Grant ATM-9732678.

PDR expresses his gratitude to Dr. Hugh Willoughby and the Hurricane Research Division (HRD) of AOML for partially supporting travel and lodging during visits to the lab over two summers, during which time research on this project was undertaken. Everyone at HRD went out of their way to provide newcomers to hurricane radar observations with valuable insight and stimulating discussions. Discussions with Drs. Sarah Jones, William Frank, Dominique Möller, Lloyd Shapiro, and Wen-Chau Lee have also been helpful. We thank Mr. Matthew Eastin and Dr. James Kossin for their insight into the flight-level data and for showing us preliminary results from a study in progress using in situ flight-level data for multiple hurricane cases. We thank Dr. Janice Enagonio for help with an omega-solver used to validate the \mathbf{Q} -vector solution. Finally, we thank Ms. Holly Snell for beneficial discussions on the spindown dynamics of hurricane-like vortices.

APPENDIX A

Q-Vector Diagnostic

In cylindrical coordinates (r, λ, z) the geostrophic radial and tangential winds are

$$u = \frac{-2Rv_{\max}\alpha z \sin\lambda}{R^2 + (r \cos\lambda - \alpha z)^2 + (r \sin\lambda)^2} + U_e(z) \cos\lambda, \quad \text{and} \\ v = \frac{2Rv_{\max}(r - \alpha z \cos\lambda)}{R^2 + (r \cos\lambda - \alpha z)^2 + (r \sin\lambda)^2} - U_e(z) \sin\lambda. \quad (\text{A1})$$

Substituting (u, v) into (7) we obtain the radial and azimuthal components of the \mathbf{Q} vector. Taking the horizontal divergence of \mathbf{Q} in cylindrical coordinates and defining nondimensional parameters, $b = r/R$ and $a = \alpha z/R$, yields

$$\nabla \cdot \mathbf{Q} = \frac{16f^3 \text{Ro}}{R(1 + b^2 + a^2 - 2ab \cos\lambda)^4} \left\{ (a\text{Ro})(2b - b^3 + 2ab^2 \cos\lambda - a^2b) \sin\lambda \right. \\ \left. - \frac{1}{f} \left(\frac{\partial U_e}{\partial z} \right) [(1 + b^2)b \cos\lambda - a(1 + b^2 + 2b^2 \cos^2\lambda) + 3a^2b \cos\lambda - a^3] \right\}. \quad (\text{A2})$$

This expression for $\nabla \cdot \mathbf{Q}$ is defined in a cylindrical coordinate system whose origin is the vortex center on the lowest surface, $z = 0$. Thus, as the tilt (i.e., αz) becomes large, harmonics other than wavenumber 1 will attain significance in the expression for $\nabla \cdot \mathbf{Q}$ in this coordinate system. If we instead transform to a coordinate system (r', λ', z) in which the origin at each level is the vortex center at that level, that is, let

$$r' \sin\lambda' = r \sin\lambda \quad -r' \cos\lambda' = \alpha z - r \cos\lambda, \quad (\text{A3})$$

then the simpler and more concise expression for $\nabla \cdot \mathbf{Q}$ given in (8) is obtained, which projects only onto wavenumber 1.

APPENDIX B

Nondivergent Barotropic Eigenanalysis

We begin with the linearized vertical vorticity equation for two-dimensional barotropic nondivergent flow:

$$\left(\frac{\partial}{\partial t} + \bar{\Omega} \frac{\partial}{\partial \lambda} \right) \left[\frac{1}{r} \frac{\partial}{\partial r} \left(r \frac{\partial \psi'}{\partial r} \right) + \frac{1}{r^2} \frac{\partial^2 \psi'}{\partial \lambda^2} \right] - \frac{1}{r} \frac{\partial \psi'}{\partial \lambda} \frac{d\bar{\zeta}}{dr} = 0, \quad (\text{B1})$$

where ψ' is the perturbation streamfunction. Given the

azimuthal-mean tangential wind and vorticity profiles, solutions to (B1) of the form

$$\psi'(r, \lambda, t) = \hat{\psi}(r) e^{i(n\lambda + \nu t)} \quad (\text{B2})$$

are sought, where n is the azimuthal wavenumber, $\hat{\psi}$ the eigenstreamfunction, and ν the eigenfrequency. We require $\hat{\psi}(r)$ to vanish as $r \rightarrow 0$ and $r \rightarrow \infty$. A standard eigenvalue solver is used to perform the numerical calculations following Gent and McWilliams (1986). Independence of the solutions described in section 5 under changes to domain size and radial grid spacing have been verified.

REFERENCES

- Bender, M. A., 1997: The effect of relative flow on the asymmetric structure in the interior of hurricanes. *J. Atmos. Sci.*, **49**, 703–724.
- Black, M. L., and H. E. Willoughby, 1992: The concentric eyewall cycle of Hurricane Gilbert. *Mon. Wea. Rev.*, **120**, 947–957.
- Black, P. G., and F. D. Marks, 1991: The structure of an eyewall meso-vortex in Hurricane Hugo (1989). Preprints, *19th Conf. on Hurricanes and Tropical Meteorology*, Miami, FL, Amer. Meteor. Soc., 579–582.
- Carr, L. E., III, and R. T. Williams, 1989: Barotropic vortex stability to perturbations from axisymmetry. *J. Atmos. Sci.*, **46**, 3177–3191.
- DeMaria, M., 1996: The effect of vertical shear on tropical cyclone intensity change. *J. Atmos. Sci.*, **53**, 2076–2087.

- Eliassen, A., and M. Lystad, 1977: The Ekman layer of a circular vortex: A numerical and theoretical study. *Geophys. Norv.*, **31**, 1–16.
- Emanuel, K. A., 1986: An air–sea interaction theory for tropical cyclones. Part I: Steady-state maintenance. *J. Atmos. Sci.*, **43**, 585–604.
- Frank, W. M., and E. A. Ritchie, 1999: Effects of environmental flow upon tropical cyclone structure. *Mon. Wea. Rev.*, **127**, 2044–2061.
- Franklin, J. L., S. J. Lord, S. E. Feuer, and F. D. Marks, 1993: The kinematic structure of Hurricane Gloria (1985) determined from nested analyses of dropwindsonde and Doppler wind data. *Mon. Wea. Rev.*, **121**, 2433–2451.
- Fung, I. Y.-S., 1977: The organization of spiral rainbands in a hurricane. Ph.D. dissertation, Massachusetts Institute of Technology, 139 pp. [Available from Dept. of Meteorology, Massachusetts Institute of Technology, Cambridge, MA 02139.]
- Gall, R., J. Tuttle, and P. Hildebrand, 1998: Small-scale spiral bands observed in Hurricanes Andrew, Hugo, and Erin. *Mon. Wea. Rev.*, **126**, 1749–1766.
- Gamache, J. F., 1998: Evaluation of a fully three-dimensional variational Doppler analysis technique. Preprints, *28th Conf. on Radar Meteorology*, Austin, TX, Amer. Meteor. Soc., 422–423.
- , H. Willoughby, M. Black, and C. Samsury, 1997: Wind shear, sea surface temperature, and convection in hurricanes observed by airborne Doppler radar. Preprints, *22d Conf. on Hurricanes and Tropical Meteorology*, Fort Collins, CO, Amer. Meteor. Soc., 121–123.
- Gent, P. R., and J. C. McWilliams, 1986: The instability of barotropic circular vortices. *Geophys. Astrophys. Fluid Dyn.*, **35**, 209–233.
- Glatz, A., and R. K. Smith, 1996: Vorticity asymmetries in Hurricane Josephine (1984). *Quart. J. Roy. Meteor. Soc.*, **122**, 391–413.
- Guinn, T. A., and W. H. Schubert, 1993: Hurricane spiral bands. *J. Atmos. Sci.*, **50**, 3380–3403.
- Hasler, A. F., P. G. Black, V. M. Karyampudi, M. Jentoft-Nilsen, K. Palaniappan, and D. Chesters, 1997: Synthesis of eyewall mesovortex and supercell convective structures in Hurricane Luis with GOES-8/9 stereo, concurrent 1-min GOES-9 and NOAA airborne radar observations. Preprints, *22d Conf. on Hurricanes and Tropical Meteorology*, Fort Collins, CO, Amer. Meteor. Soc., 201–202.
- Haynes, P. H., and M. E. McIntyre, 1987: On the evolution of vorticity and potential vorticity in the presence of diabatic heating and frictional or other forces. *J. Atmos. Sci.*, **44**, 828–841.
- Hoskins, B. J., I. Draghici, and H. C. Davies, 1978: A new look at the ω -equation. *Quart. J. Roy. Meteor. Soc.*, **104**, 31–38.
- Jones, S. C., 1995: The evolution of vortices in vertical shear: Initially barotropic vortices. *Quart. J. Roy. Meteor. Soc.*, **121**, 821–851.
- Jorgensen, D. P., 1984: Mesoscale and convective-scale characteristics of mature hurricanes. Part I: General observations by research aircraft. *J. Atmos. Sci.*, **41**, 1268–1285.
- Kloosterzeil, R. C., and G. J. van Heijst, 1991: An experimental study of unstable barotropic vortices in a rotating fluid. *J. Fluid Mech.*, **223**, 1–24.
- Kuo, H.-C., R. T. Williams, and J.-H. Chen, 1999: A possible mechanism for the eye rotation of Typhoon Herb. *J. Atmos. Sci.*, **56**, 1659–1673.
- Lamb, H., 1932: *Hydrodynamics*. 6th ed. Dover, 732 pp.
- Marks, F. D., and R. A. Houze, 1984: Airborne Doppler radar observations in Hurricane Debby. *Bull. Amer. Meteor. Soc.*, **65**, 569–582.
- , —, and J. Gamache, 1992: Dual-aircraft investigation of the inner core of Hurricane Norbert: Part I: Kinematic structure. *J. Atmos. Sci.*, **49**, 919–942.
- Molinari, J., S. Skubis, and D. Vollaro, 1995: External influences on hurricane intensity. Part III: Potential vorticity structure. *J. Atmos. Sci.*, **52**, 3593–3606.
- Möller, J. D., and R. K. Smith, 1994: The development of potential vorticity in a hurricane-like vortex. *Quart. J. Roy. Meteor. Soc.*, **120**, 1255–1265.
- , and M. T. Montgomery, 1999a: Hurricane evolution via potential vorticity asymmetries in a three-dimensional asymmetric model. *23d Conf. on Hurricanes and Tropical Meteorology*, Dallas, TX, Amer. Meteor. Soc., 684–685.
- , and —, 1999b: Vortex Rossby waves and hurricane intensification in a barotropic model. *J. Atmos. Sci.*, **56**, 1674–1687.
- Montgomery, M. T., and R. Kallenbach, 1997: A theory for vortex Rossby-waves and its application to spiral bands and intensity changes in hurricanes. *Quart. J. Roy. Meteor. Soc.*, **123**, 435–465.
- , and J. Enagonio, 1998: Tropical cyclogenesis via convectively forced vortex Rossby waves in a three-dimensional quasigeostrophic model. *J. Atmos. Sci.*, **55**, 3176–3207.
- Nelder, J. A., and R. Mead, 1965: A simplex method for function minimization. *Comput. J.*, **7**, 308–313.
- Pasch, R. J., and M. Mayfield, 1996: Eastern North Pacific hurricane season of 1994. *Mon. Wea. Rev.*, **124**, 1579–1590.
- Raymond, D. J., 1992: Nonlinear balance and potential-vorticity thinking at large Rossby number. *Quart. J. Roy. Meteor. Soc.*, **118**, 987–1015.
- , and H. Jiang, 1990: A theory for long-lived mesoscale convective systems. *J. Atmos. Sci.*, **47**, 3067–3077.
- Roll, H. V., 1965: *Physics of the Marine Atmosphere*. Academic Press, 426 pp.
- Roux, F., and N. Viltard, 1995: Structure and evolution of Hurricane Claudette on 7 September 1991 from airborne Doppler radar observations. Part I: Kinematics. *Mon. Wea. Rev.*, **123**, 2611–2639.
- , and F. D. Marks, 1996: Extended velocity track display (EVTD): An improved processing method for Doppler radar observations of tropical cyclones. *J. Atmos. Oceanic Technol.*, **13**, 875–899.
- Schubert, W. H., M. T. Montgomery, R. K. Taft, T. A. Guinn, S. R. Fulton, J. P. Kossin, and J. P. Edwards, 1999: Polygonal eyewalls, asymmetric eye contraction and potential vorticity mixing in hurricanes. *J. Atmos. Sci.*, **56**, 1197–1223.
- Shapiro, L. J., 1983: The asymmetric boundary layer flow under a translating hurricane. *J. Atmos. Sci.*, **40**, 1984–1998.
- , and M. T. Montgomery, 1993: A three-dimensional balance theory for rapidly rotating vortices. *J. Atmos. Sci.*, **50**, 3322–3335.
- Shay, L. K., G. J. Goni, F. D. Marks, J. J. Cione, and P. G. Black, 1998: Role of warm ocean features on intensity change: Hurricane Opal. Preprints, *Special Session on Tropical Cyclone Intensity Changes*, Phoenix, AZ, Amer. Meteor. Soc., 131–138.
- Simpson, R. H., and R. H. Riehl, 1958: Mid-tropospheric ventilation as a constraint on hurricane development and maintenance. *Proc. Tech. Conf. on Hurricanes*, Miami Beach, FL, Amer. Meteor. Soc., D4.1–D4.10.
- Smith, G. B., and M. T. Montgomery, 1995: Vortex axisymmetrization: Dependence on azimuthal wavenumber or asymmetric radial structure changes. *Quart. J. Roy. Meteor. Soc.*, **121**, 1615–1650.
- Smith, R. A., and M. N. Rosenbluth, 1990: Algebraic instability of hollow electron columns and cylindrical vortices. *Phys. Rev. Lett.*, **64**, 649–652.
- Snell, H. D., and M. T. Montgomery, 1999: Spin-down dynamics of axisymmetric hurricanes. *23d Conf. on Hurricanes and Tropical Meteorology*, Dallas, TX, Amer. Meteor. Soc., 1031.
- Sutyrin, G. G., 1989: Azimuthal waves and symmetrization of an intense vortex. *Sov. Phys. Dokl.*, **34**, 104–106.
- Trier, S. B., C. A. Davis, and W. C. Skamarock, 1998: Influence of mesoconvective vortices on the environment of deep convection. Preprints, *19th Conf. on Severe Local Storms*, Minneapolis, MN, Amer. Meteor. Soc., 36–39.
- Willoughby, H. E., 1979: Forced secondary circulations in hurricanes. *J. Geophys. Res.*, **84**, 3173–3183.
- , and M. B. Chelmon, 1982: Objective determination of hurricane tracks from aircraft observations. *Mon. Wea. Rev.*, **110**, 1298–1305.
- , F. D. Marks, and R. J. Feinberg, 1984: Stationary and propagating convective bands in asymmetric hurricanes. *J. Atmos. Sci.*, **41**, 3189–3211.